

1 Atmospheric ammonia variability and link with PM formation: a
2 case study over the Paris area

3 Viatte Camille¹, Wang Tianze¹, Van Damme Martin², Dammers Enrico³, Meleux Frederik⁴,
4 Clarisse Lieven², Shephard Mark W.³, Whitburn Simon², Coheur Pierre François², Cady-Pereira
5 Karen E.⁵, and Clerbaux Cathy^{1,2}

6 ¹ LATMOS/IPSL, Sorbonne Université, UVSQ, CNRS, Paris, France

7 ² Université libre de Bruxelles (ULB), Service de Chimie Quantique et Photophysique, Atmospheric
8 Spectroscopy, Brussels, Belgium

9 ³ Environment and Climate Change Canada, Toronto, Ontario, Canada

10 ⁴ Institut national de l'environnement industriel et des risques, INERIS, Verneuil en Halatte, France

11 ⁵ Atmospheric and Environmental Research (AER), Inc., Lexington, USA

12 Abstract

13 The Paris megacity experiences frequent particulate matter ($PM_{2.5}$, PM with a diameter less than
14 $2.5 \mu m$) pollution episodes in springtime (March-April). At this time of the year, large parts of
15 the particles consist of ammonium sulfate and nitrate which are formed from ammonia (NH_3)
16 released during fertilizer spreading practices and transported from the surrounding areas to
17 Paris. There is still limited knowledge on the emission sources around Paris, their magnitude and
18 seasonality.

19 Using space-borne NH_3 observation records of 10-years (2008-2017) and 5-years (2013-2017)
20 provided by the Infrared Atmospheric Sounding Interferometer (IASI) and the Cross-Track
21 Infrared Sounder (CrIS) instrument, regional pattern of NH_3 variabilities (seasonal and inter-
22 annual) are derived. Observations reveal identical high seasonal variabilities with three major
23 NH_3 hot spots found from March to August. The high inter-annual variability is discussed with
24 respect to atmospheric total precipitation and temperature.

25 A detailed analysis of the seasonal cycle is performed using both IASI and the CrIS instrument
26 data, together with outputs from the CHIMERE atmospheric model. For 2014 and 2015 the
27 CHIMERE model shows coefficient of determination of 0.58 and 0.18 when comparing with IASI
28 and CrIS, respectively. It is found that the model is only able to reproduce half of the observed
29 atmospheric temporal NH_3 variability in the domain. In term of spatial variability, the CHIMERE
30 monthly NH_3 concentrations in springtime show a slight underrepresentation over Belgium and
31 the United-Kingdom and overrepresentation in agricultural areas in the French Brittany/Pays de
32 la Loire and Plateau du Jura region, as well as in the north part of Switzerland. In addition, $PM_{2.5}$
33 concentrations derived from the CHIMERE model have been evaluated against surface
34 measurements from the Airparif network over Paris. Agreement was found (r^2 of 0.56) with
35 however an underestimation during spring pollution events.

36 Using HYSPLIT cluster analysis of back-trajectories, we show that NH_3 total columns measured in
37 spring over Paris are enhanced when air masses are originated from the Northeast (e. g.,
38 Netherlands and Belgium), highlighting the long-range transport importance on the NH_3 budget
39 over Paris. Variability of NH_3 in the Northeast region is likely to impact NH_3 concentrations in the
40 Parisian region since the cross-correlation function is above 0.3 (at lag = 0 and 1).

41 Finally, we quantify the key meteorological parameters driving the specific conditions important
42 for the $PM_{2.5}$ formation from NH_3 in the Ile-de-France region in springtime. Data-driven results
43 based on surface $PM_{2.5}$ measurements from the Airparif network and IASI NH_3 observations
44 show that a combination of the factors, e. g. a low boundary layer of $\sim 500m$, a relatively low
45 temperature of $5^\circ C$, a high relative humidity of 70%, and wind from the Northeast contributes to
46 favor $PM_{2.5}$ and NH_3 correlation.

47 1. Introduction

48 Ammonia (NH₃) is an atmospheric pollutant and one of the main sources of reactive nitrogen in
49 the atmosphere which is involved in numerous biogeochemical exchanges impacting all
50 ecosystems [Sutton et al., 2013]. The global budget of reactive N has dramatically increased
51 since the preindustrial era [Holland et al., 2005; Battye et al., 2017] causing major
52 environmental damages such as ecosystems and species extinction [Isbell et al., 2013;
53 Hernandez et al., 2016], as well as soil and water eutrophication and acidification [Rockström et
54 al., 2009]. NH₃ is a precursor of ammonium salts which can form up to 50% to particulate matter
55 (PM) total mass [Behera et al., 2013]. Large cities such as Paris (which is the most populated
56 area in the European Union with 10.5 million people when its larger metropolitan regions are
57 included) typically experiences strong PM pollution episodes in springtime. These particles are
58 known to be harmful for human health [Pope III et al., 2009] inducing 2000 deaths per year in
59 the Paris megacity [Corso et al., 2016] and to impact the radiative budget of the Earth [Myhre et
60 al., 2013].

61 Because of their impact on the environment, public health, and climate change, NH₃ emissions
62 are regulated in several countries in the world. However, NH₃ emissions of European countries
63 have increased by 2% over the period 2014-2016 [National Emission Ceilings Directive reporting
64 status, 2018], where the Gothenburg Protocol set a reduction of 6% by 2020. In France, where
65 94% of NH₃ emissions come from the agriculture sector [CITEPA, 2018] as a result of extensive
66 fertilizer use to increase crop yields [Erisman et al., 2008], policies have been implemented with
67 the aim to reduce NH₃ emissions by 13% in 2030 relative to 2005 [CEIP, 2016]. However NH₃
68 emissions are projected to increase in the future globally with increased population and food
69 demand [van Vuuren et al., 2011] and NH₃ volatilization will be enhanced with climate change
70 [Sutton et al., 2013].

71 Once in the atmosphere, NH₃ is rapidly removed by wet and dry deposition, and by reactions
72 with atmospheric sulfuric and nitric acid, leading to a relatively short lifetime between a few
73 hours and few days [Galloway et al., 2003]. Release of NH₃ in the atmosphere depends on i)
74 agriculture practices: spreading season, fertilizer form (urea, ammonium nitrate), fertilizer
75 application methods, crops, soil conditions such as pH [Hamaoui-Laguel et al., 2014]; and on ii)
76 meteorological conditions (i.e. wind, temperature, and precipitation). Inter-annual variability of
77 PM formation over urban area is poorly understood, since it also depends on many factors such
78 as atmospheric humidity and temperature, which govern the phase equilibrium of secondary
79 aerosols [Fuzzi et al., 2015]. The variety of factors influencing NH₃ volatilization and PM
80 formation illustrates the complexity of predicting their concentrations in the atmosphere
81 [Behera et al., 2013].

82 Atmospheric chemical transport models have difficulty representing both NH_3 and $\text{PM}_{2.5}$
83 distributions due to the challenge of reproducing NH_3 temporal variability [Pinder et al., 2006;
84 Fortems-Cheiney et al., 2016], long-range transport of pollutants [Moran et al., 2014], and
85 secondary aerosol formation in the atmosphere [Petetin et al., 2016]. The GEOS-Chem chemical
86 transport model [Bey et al., 2001] was found to underestimate the observed NH_3 concentrations
87 in most regions of the globe [Zhu et al., 2013; Li et al., 2017]. Heald et al. (2012) compared the
88 IASI observations with the GEOS-Chem model and showed that NH_3 is likely underestimated in
89 California, leading to a local underestimate of ammonium nitrate aerosol. Similarly, the French
90 CHIMERE model [Menut et al., 2013] underestimates the NH_3 budget over Paris [Petetin et al.,
91 2016; Fortems-Cheiney et al., 2016] because of the mis-representation of agricultural emissions
92 in terms of intensity and both spatial and temporal distribution. Often ground and aircraft-
93 based observations are used to provide detailed representation of the atmospheric state that
94 can be used to evaluate and improve the model simulations; however, these can be spatially
95 sparse and/or over short sampling periods, especially globally. Additionally, more recently
96 available (within the last 10-years) sun-synchronous satellite-based infrared sensors have been
97 providing NH_3 observations globally with a spatial resolution of ~ 15 km approximately twice a
98 day. These satellite observations have limited independent vertical information, but do capture
99 the spatiotemporal variabilities needed to help address these issues and improve model
100 simulations, especially in remote locations [Skj th et al., 2011; Kranenburg et al., 2016].

101 Aside from the Tropospheric Emission Spectrometer (TES, [Beer et al., 2008]), now
102 decommissioned but which was first to demonstrate the capability of thermal infrared
103 instruments to monitoring lower tropospheric NH_3 , 3 missions are able to measure it now : the
104 Atmospheric InfraRed Sounder (AIRS, [Warner et al., 2016]), the Cross-track Infrared Sounder
105 (CrIS, [Shephard and Cady-Pereira, 2015]), and the Infrared Atmospheric Sounding
106 Interferometer (IASI, [Clarisse et al., 2009]). Recent studies have shown the increased capacity
107 of space-borne instruments to derived spatial and seasonal distributions of NH_3 concentrations
108 globally [Clarisse et al., 2009; Shephard et al., 2011; Van Damme et al., 2014a & 2015a],
109 regionally [Beer et al., 2008; Clarisse et al., 2010; Van Damme et al., 2014b] and locally [Van
110 Damme et al., 2018], as well as trends of NH_3 [Warner et al., 2017].

111 Representative measurements of NH_3 concentrations and spatiotemporal variabilities are
112 needed to address the link between NH_3 and $\text{PM}_{2.5}$ formation and improve model simulations.
113 This has been attempted previously in some cities around the world, such as in Shanghai [Ye et
114 al., 2011], Houston [Gong et al., 2013], Santiago City [Toro et al., 2014], and Beijing [Zhao et al.,
115 2016] for instance. However, although the Paris megacity is repeatedly shrouded by particulate
116 pollution episodes, many studies are limited in the Paris megacity and performed over relatively
117 short time frame during field campaigns: NH_3 measurements from May 2010 to February 2011
118 [Petetin et al., 2016] and nitrate, sulfate, and ammonium aerosol measurements in July 2009

119 [Zhang et al., 2013], or based on numerical simulations [Skyllakou et al., 2014]. Our study is a
120 data-driven regional approach and considers a longer time period to study the seasonal/inter-
121 annual variabilities of NH_3 and its impact of $\text{PM}_{2.5}$ formation over the Paris megacity. Specifically
122 in this paper we study concentrations and spatiotemporal variability of atmospheric NH_3 from
123 the agricultural sector to gain insights on its effects on megacity air quality using: 1) long-term
124 satellite observations derived from IASI (10 years from 2008 to 2017) and CrIS (5 years from
125 2013 to 2017) at regional scale (400km radius-circle from Paris city center); 2) spatiotemporal
126 patterns of the CHIMERE model evaluated against the IASI and CrIS datasets for 2014 and 2015;
127 and 3) the main meteorological parameters favoring the secondary $\text{PM}_{2.5}$ formation from NH_3 in
128 the Paris megacity are analyzed.

129 2. Methodology

130 2.1. Region of analysis

131 The domain of analysis covers a circular area of 400 km radius around the Paris city center
132 (Figure 1, larger circle) enabling the study of temporal and spatial variabilities of NH_3 emission
133 sources likely to affect air quality in the Paris megacity. It has been selected for two reasons.
134 First, it includes main regions known for their high NH_3 emissions, which can be transported and
135 affect air quality over the Parisian region (Ile-de-France -IdF-, smaller circle in Figure 1).
136 Emission regions in the Netherlands, North of Germany, Northwest of Belgium, and the Brittany
137 region in France, are highlighted in darker colors in Figure 1 (emissions values are from the
138 European Monitoring and Evaluation Programme -EMEP- 2015). Second, this area corresponds
139 to the transport of 24 hours back-trajectories from Paris generated from the HYSPLIT model for
140 one year, ensuring that NH_3 can indeed be efficiently transported from the emitting sources
141 within the selected domain to the IdF region.

142 2.2. Satellite observations of ammonia

143 For this study we used the available data from IASI and CrIS which are both Fourier transform
144 spectrometers to evaluate the current capacity to observe NH_3 concentrations from space, and
145 study its variability around IdF. Technical information are summarized in Table 1.

146 2.2.1. Infrared Atmospheric Sounding Interferometer (IASI)

147 IASI is a nadir-viewing spectrometer launched on board the Metop-A and Metop-B satellites and
148 operated by EUMETSAT (European Organisation for the Exploitation of Meteorological
149 Satellites), since October 2006 and September 2012, respectively. These satellites are on similar
150 polar orbits with Equator crossing times at 09:30 (21:30) local mean solar time for the
151 descending (ascending) orbit. IASI measures the thermal infrared radiation of the system Earth-
152 atmosphere in the spectral range from 645 to 2760 cm^{-1} with a spectral resolution 0.5 cm^{-1}

153 apodized. The satellite swath is an area of 2200 km width composed by off-nadir measurements
154 up to 48.3° on both sides of the track. At nadir, the IASI field of view is composed of 4 x 4 pixels
155 of 12 km diameter each [Clerbaux et al., 2009].

156 The NH_3 total columns used here are derived from IASI using an Artificial Neural Network
157 reanalyzed with ERA-interim data (ANNI-NH3-v2.1R [Van Damme et al., 2017]). This dataset is
158 consistent in time and suitable for investigating inter-annual variability, which is one purpose of
159 this study. Note that we have considered here only morning measurements (9:30) since the
160 evening ones (21:30) are associated with larger relative errors [Van Damme et al., 2017]. IASI
161 retrievals provide a robust error estimate for each IASI-NH3 observations, allowing to take into
162 account the variable sensitivity when comparing IASI dataset with independent measurements.
163 Finally, no filter on relative errors of the IASI datasets has been applied following
164 recommendations from Van Damme et al. (2017) and outliers for which concentrations exceed
165 10 standard deviations above the mean in the domain of study have been removed.

166 Over the studied area, Metop-A and Metop-B have an overpass time difference ranging from
167 only a few seconds to 67 minutes depending on the viewing geometry of the satellite scans; the
168 average difference is 26 minutes for the 1325 days of common measurements. Monthly maps
169 for the 10 years of observations between 2008 and 2017 are obtained by averaging Metop-A and
170 whenever Metop-B (the two instruments are considered jointly for their period of common
171 operation from March 2013 to 2017) with more than 10^5 pixels on average over the domain of
172 analysis. The number of available NH_3 columns depends not only on the satellite overpass time
173 but also on the state of the atmosphere being remotely sensed (e.g. thermal contrast and cloud
174 cover). IASI NH_3 has been evaluated using the LOTOS-EUROS model over Europe [Van Damme et
175 al., 2014b] and ground-based and airborne measurements [Van Damme et al., 2015b], showing
176 consistency between the IASI NH_3 and the available datasets. When comparing IASI NH_3
177 (previous IASI-NN version) with ground-based Fourier transform infrared (FTIR) observations, a
178 correlation of 0.8 and a slope of 0.73, with a mean relative difference of $-32.4 \pm (56.3)\%$ have
179 been found [Dammers et al., 2016].

180 2.2.2. Cross-track Infrared Sounder (CrIS)

181 The CrIS instrument [Zavalyov et al., 2013] is a Fourier Transform spectrometer operated by the
182 Joint Polar Satellite System (JPSS) program on Suomi National Polar-orbiting Partnership (NPP)
183 satellite, launched on 28 October 2011. CrIS is in a sun-synchronous orbit with a mean local
184 daytime overpass time of 13:30 (01:30) in the ascending (descending) node. CrIS measures the
185 atmospheric composition over three wavelength bands in the infrared region ($645\text{--}1095\text{ cm}^{-1}$;
186 $1210\text{--}1750\text{ cm}^{-1}$; $2155\text{--}2550\text{ cm}^{-1}$). NH_3 retrievals are performed from the $645\text{--}1095\text{ cm}^{-1}$ band
187 with a spectral resolution of 0.625 cm^{-1} . The CrIS instrument scans a 2200 km swath width (+/-

188 50 °). At nadir, the CrIS field of view consists of a 3 × 3 array of circular pixels of 14 km diameter
189 each.

190 The CrIS Fast Physical Retrieval (CRPR) [Shephard and Cady-Pereira., 2015] uses an optimal
191 estimation approach [Rodgers, 2000] that minimizes the difference between the CrIS measured
192 atmospheric spectra and a very fast Optimal Spectral Sampling (OSS) [Moncet et al., 2008]
193 forward model simulated spectrum to retrieve atmospheric profiles of ammonia volume mixing
194 ratios. This physical approach provides direct estimates of the retrieval errors and the vertical
195 sensitivity (averaging kernels) of the satellite observations, which is important as they vary from
196 profile-to-profile depending on the atmospheric state. The retrieved error covariance and
197 averaging kernels are also beneficial for air quality model comparisons and data assimilation
198 into models as any *a priori* information used in the retrieval can be accounted for in a robust
199 manner (i.e. observation operator). CrIS has been shown to retrieve ammonia surface
200 concentrations values down to ~0.2-0.3 ppbv under favorable conditions [Kharol, et al., 2018].
201 CrIS comparisons with ground-based FTIR observations show a correlation of 0.77 with a low
202 CrIS bias of +2% in the total column [Dammers et al., 2017]. Initial evaluation against surface
203 observations from the Ammonia Monitoring Network (AMoN) show that even with the inherent
204 sampling differences between the two surface observations they compare well with a
205 correlation of 0.76 and an overall mean CrIS – AMoN difference of ~+15% [Kharol et al., 2018].

206 For this study, the CrIS quality flag = 4 has been used, ensuring that retrievals provide some
207 information from the measurement (degrees-of-freedom- of-signal – DOFS > 0.1). In addition,
208 outliers for which concentrations exceed 10 standard deviations above the mean have been
209 removed.

210 2.3. Modelling NH₃ from the CHIMERE model

211 The CHIMERE runs used in this study were obtained in the framework of the Copernicus
212 Atmospheric Monitoring Service (CAMS, <https://atmosphere.copernicus.eu/>), and its annual
213 task devoted to the production of regional reanalysis over Europe. The hindcasts for year 2014
214 and 2015 (raw simulation without data assimilation) were produced over Europe with a
215 horizontal resolution of 0.1° per 0.1° and
216 9 vertical levels stretched from the surface up to 500 hPa (~5000m). The input data to feed
217 CHIMERE [Menut et al., 2013; Mailler et al., 2017] were the Integrated Forecasting System (IFS)
218 meteorological data from European Centre for Medium-Range Weather Forecasts (ECMWF), the
219 annual emission inventory provided by the Netherlands Organisation for Applied Scientific
220 Research (TNO) [Kuenen et al., 2014] for year 2011. These annual emissions are then distributed
221 in hourly data to feed CHIMERE using seasonal, weekly and hourly factors. Fire emissions come
222 from the Global Fire Assimilation System (GFAS, [Kaiser et al., 2012]).

223 The model computes hourly concentrations for more than 180 species, among which are the
224 regulated pollutants such as ozone, PM₁₀, and NH₃. The processes that will influence the NH₃
225 concentrations taken into consideration in CHIMERE are the dry deposition (following [Wesely
226 et al., 1989] and wet deposition due to in-cloud process and precipitations. The gas-particulate
227 phase equilibrium is computed with the ISOROPPIA module [Nenes et al, 1998] which is a
228 thermodynamic equilibrium model for NH₄⁺, NO₃⁻ and SO₄²⁻. It evaluates the NH₄NO₃
229 contribution to the particulate matter which is especially large during March-April pollution
230 episodes [Petit et al., 2017].

231 These datasets were evaluated over Europe for several pollutants before being used for air
232 quality studies (<http://policy.atmosphere.copernicus.eu/Reports.html>).

233 The model NH₃ profiles were integrated vertically along the 9 km model layers to provide a
234 column that can be compared to that of the satellite measurements. Concretely this makes the
235 reasonable assumption that all the NH₃ is located within this 0-5km layer (see e.g. Figure 1 in
236 [Whitburn et al., 2016]).

237 To evaluate the model capacity of reproducing NH₃ variability in space and time at regional scale
238 and its impact on air quality at local scale, comparisons have been performed in 2014 and 2015
239 for the following reasons. At regional scale (over the 400 km radius around Paris), NH₃ total
240 columns derived from IASI in 2014 and 2015 are highly variable in spring, reaching 10% higher in
241 March and 50% lower in May than the 10-years average. Since ammonia emission variability in
242 France depends on seasonal timing of fertilizer applications [Ramanantenasoa et al., 2018], this
243 period is crucial to assess the model capacity. Second, the IdF region (100 km radius around
244 Paris) also experiences high NH₃ and PM_{2.5} events in spring 2014 and 2015 (Figure S1). Thus,
245 these years serve as benchmark to evaluate the model in terms of NH₃ variability and PM_{2.5}
246 formation at local and regional scales.

247 2.4. Relative scales and coincidence criteria for dataset comparisons

248 Direct quantitative comparisons of satellite NH₃ products are difficult because of the different
249 overpass times and ground footprint sizes of the 2 space borne instruments, which are not
250 compatible with the high variability of NH₃ in space and time. Therefore, the evaluation of
251 satellite observations is often made with the use of in situ measurements performed at surface
252 and onboard aircrafts [Nowak et al., 2012; Van Damme et al., 2015b], or with ground-based
253 remote-sounding FTIR [Dammers et al., 2016; Dammers et al., 2017].

254 The purpose here of comparing CrIS and IASI is to assess qualitatively the spatiotemporal
255 patterns of the NH₃ sources derived from the two datasets and use these regional observations
256 to evaluate the CHIMERE model in the domain of analysis at the local time for their respective
257 overpasses: 9:30 and 13:30. CHIMERE outputs, in terms of NH₃ concentrations, have already

258 been compared to the IASI observations at regional scale (Europe, [Fortems-Cheiney et al.,
259 2016], and to surface measurements at local scale (Paris, [Petetin et al., 2016]), but have never
260 been evaluated against the CrIS observations.

261 One aspect that needs to be considered when comparing concentration amounts inferred from
262 infrared satellite observations is the importance of the algorithm and the a priori information
263 used in the retrieval, especially for NH₃ which has limited vertical information. Some differences
264 between the IASI and CrIS observations might arise due to instrument measurement differences
265 (e.g. sensitivity), difference sampling period (e.g. overpass times of morning/evening vs middle
266 of day/night), and retrieval algorithm differences, but they have both been validated and shown
267 to capture well the spatiotemporal variations in lower tropospheric ammonia. Since the purpose
268 of our study is not to quantitatively compare IASI and CrIS NH₃ data, but rather to use these
269 independent datasets to assess NH₃ sources patterns over the domain and qualitatively
270 evaluate the CHIMERE model in term of NH₃ concentrations and variabilities, a standardization
271 procedure was applied to their retrieved absolute NH₃ columns. We computed “standardized
272 columns” for each independent dataset (IASI, CrIS, and CHIMERE, separately) for 2014 and 2015
273 over the domain of study in such a way that the corresponding values have a standard deviation
274 of 1 and a mean of 0, as in [Wilks, 2011].

275 The standardized columns have been computed following equation 1:

$$276 \quad X_{stand}^{data} = \frac{(X^{data} - \mu(X^{data}))}{S(X^{data})} \quad (1)$$

277 Where $(X^{data}) = \frac{1}{N} \sum_{i=1}^N X_i^{data}$, $S(X^{data}) = \sqrt{\frac{1}{N-1} \sum_{i=1}^N (X_i - \mu)^2}$, X^{data} corresponds to NH₃
278 columns derived from a dataset (IASI, CrIS, or CHIMERE), and X_{stand}^{data} is the corresponding
279 standardized dataset.

280 In addition, to compare CHIMERE outputs with satellite data/columns, spatial and temporal
281 coincidence criteria have been applied. To compare satellite observations, all CrIS pixels located
282 within a 25-km radius circle from the center of the IASI ground pixels have been considered
283 within the same day of measurements. A spatial criterion of 25 km has been chosen because it
284 optimizes the number of pairs involved in the statistics and improves the correlations. As for the
285 comparisons between the model and the observations: all CHIMERE outputs located within the
286 same 0.15°x0.15° grid box than the satellite and within 1 hour from its measurement have been
287 selected.

288 3. Results

289 3.1. NH₃ regional observations derived from IASI (10-years) and CrIS (5- 290 years)

291

3.1.1. Seasonal variabilities

292 First the seasonal variability was investigated over the IdF area. On a monthly basis, the 10-year
293 and 5-year averaged regional NH₃ total column distributions derived from IASI and CrIS were
294 found to exhibit a high seasonality over the domain (Figures 2 and 3). Note that the distributions
295 in Figures 2 and 3 have been obtained by averaging satellite NH₃ observations in 0.25°x 0.25°
296 grid boxes. Both satellite datasets exhibits the same variability over the domain even if the time
297 period is different (10-years versus 5-years) and the sampling hour differs (~9.30 versus ~13.30).
298 One note that CrIS and IASI NH₃ columns present small differences in term of NH₃ total columns
299 in low concentration regimes in the domain of study.

300 In these figures (2 and 3) high NH₃ concentrations (up to 2.10¹⁶ molecules/cm²) can be observed
301 from March to August at different locations of the domain:

- 302 • The French Champagne-Ardennes region in March and April (Figures 2 and 3, box A),
- 303 • The northern part of the domain corresponding to the Netherlands and the North of Belgium
304 from April to August (Figures 2 and 3, box B), and
- 305 • The Brittany/Pays de la Loire regions (West of France) mainly in April and August but still
306 persistent from March to August (Figures 2 and 3, box C).

307 The observed seasonality is mainly related to agricultural practices (fertilizer application period
308 varying as function of the crop types and type of livestock) and changes in temperatures, with
309 higher temperatures favoring volatilization. This likely explains the high concentration in July
310 and August.

311 In the Champagne-Ardennes region, areas of hotspots do not correspond to vineyards but to
312 field vegetables and root crops ([https://agriculture.gouv.fr/overview-french-agricultural-](https://agriculture.gouv.fr/overview-french-agricultural-diversity)
313 [diversity](https://agriculture.gouv.fr/overview-french-agricultural-diversity), and AGRESTE, Service Central d'Enquêtes et d'Études Statistiques, 2015
314 <http://agreste.agriculture.gouv.fr/IMG/pdf/R4215A15.pdf>). This is a leader region for mineral
315 fertilization used for sugar industry in France [Ramanantenasoa et al., 2018]. Hamaoui-Laguel et
316 al. (2014) and Fortems-Cheiney et al. (2016) have previously noted that NH₃ emissions in this
317 region, mainly due to fertilizer over barley, sugar beet, and potato starch in early March, were
318 higher than what have been reported in the EMEP inventory.

319 NH₃ concentrations are high from April to August in the northern part of the domain that is
320 known for its animal farming (Eurostat 2014, [http://ec.europa.eu/eurostat/statistics-](http://ec.europa.eu/eurostat/statistics-explained/index.php?title=File:Livestock_density_by_NUTS_2_regions,_EU-28,_2013.png)
321 [explained/index.php?title=File:Livestock_density_by_NUTS_2_regions,_EU-28,_2013.png](http://ec.europa.eu/eurostat/statistics-explained/index.php?title=File:Livestock_density_by_NUTS_2_regions,_EU-28,_2013.png), [Van
322 Damme et al., 2014a; Scarlet et al., 2018 – their figure 2]).

323 In the Pays de la Loire, NH₃ concentrations are high in April and August and remain relatively
324 high from March to September. Hotspots are found in areas of livestock farming, mainly poultry

325 [Robinson et al., 2014 - their figure 2c], which might explain the high and relatively constant NH₃
326 concentrations over warmer periods in this region.

327 3.1.2. Inter-annual variabilities

328 As can be seen in Figures 2 and 3, NH₃ concentrations are enhanced between March and August
329 in the domain. In this section, inter-annual variabilities are discussed regarding meteorological
330 conditions and agricultural practices during this time period.

331 Inter-annual variability of NH₃ is higher in springtime than in summer, e.g. in June the variance is
332 8 times lower than for the other months. To illustrate the inter-annual variability in springtime,
333 maps of monthly mean NH₃ total columns derived in March-April period from IASI (2008-2017
334 time period) and from CrIS (2013-2017 time period) are shown in Figure 4. Both satellite
335 distributions exhibit the same inter-annual variability from 2013 to 2017 with higher NH₃
336 concentrations in 2015 over the northern part of the domain than the other years. NH₃
337 concentrations derived from IASI in 2011 are 150% higher in spring (March and April) compared
338 to 2016 (Figure 4). It has been recently shown that spatial variability of NH₃ emissions in France
339 is due to fertilizer use and type and pedoclimatic conditions, and that temporal variability
340 depends on seasonal timing of fertilizer applications [Ramanantenasoa et al., 2018]. In addition,
341 inter-annual variabilities of NH₃ concentrations over the United-States are dominated by
342 meteorological conditions [Schiferl et al., 2016]. Thus, inter-annual variability of observed NH₃
343 total columns is likely to be driven by meteorological conditions and specific agricultural
344 constrains (crop type and phenological stage for instance).

345 To investigate the impact of meteorological conditions on atmospheric NH₃ variability, we
346 computed the monthly mean anomalies of total precipitation versus skin temperature derived
347 from ECMWF ERA-interim [Dee et al., 2011], color coded by NH₃ total columns anomalies
348 derived from IASI, as shown in Figure 5. Monthly mean anomalies have been calculated relative
349 to the 10-years averages (in %). In this figure, monthly NH₃ total columns are at least 10% higher
350 (positive anomalies, red dots) when skin temperatures are higher and total precipitation are
351 lower than the 10-year average. In contrast, negative monthly NH₃ total columns anomalies
352 (blue dots, Figure 5) are associated with higher total precipitation and lower skin temperatures
353 than the 10-years average. To further detail this analysis, Figure 1 of the supplement
354 information shows bar plots of monthly mean NH₃ total columns derived from IASI, total
355 precipitation and skin temperature derived from ECMWF from March to August, plotted in
356 different colors for the different years of measurements from 2008 to 2017. NH₃ total columns
357 are larger by more than 300% in March-April 2012 compared to 2013 (Figure S2a). Total
358 precipitation is higher (0.4 mm compared to 1 mm, Figure S2b) and skin temperature is lower
359 (281 compared to 288 K, Figure S2c) in March 2013 than in March 2012 on average over the
360 domain. Overall, total precipitation is anti-correlated with NH₃ concentrations in the

361 atmosphere ($R = -0.52$ from March to May for all years, not shown here) likely because of a) the
362 wet deposition importance in the atmospheric NH_3 removal and b) the absence of fertilization
363 during rainy periods. Skin temperature is relatively correlated with NH_3 concentrations ($R = 0.30$
364 from March to May for all years) since higher temperature increases volatilization of NH_3 from
365 the surface to the atmosphere.

366 In addition, NH_3 concentration is maximum in March 2011 whereas it peaks later in April for
367 2012 (Figure S2a). Springtime is a spreading fertilizer period depending on many agricultural and
368 meteorological constrains. When temperature are mild, such as in 2012 (Figure S2b), fertilizer
369 spreading may occur sooner because the phenological growth stage might be more advanced.
370 Fertilizing process period also varies in function of the sowing date which depends on
371 agricultural practices and crop types: corn is fertilized in early spring whereas rapeseed is in late
372 spring.

373 Overall, all these meteorological (precipitation and temperature) and agricultural (fertilizer and
374 manure applications) parameters are possible factors to account for the high NH_3 inter-annual
375 variabilities revealed by both IASI and CrIS in the domain of study.

376 3.2. Comparisons of NH_3 columns derived from IASI, CrIS, and CHIMERE 377 for 2014 and 2015

378 To discuss the representation of agricultural emissions in the models in terms of intensity and
379 both spatial and temporal distributions, regional satellite observations derived from IASI and
380 CrIS have been compared to the CHIMERE model in the region of analysis.

381 3.2.1. Annual cycle

382 Standardized monthly mean concentrations derived from IASI, CrIS, and CHIMERE for 2014 and
383 2015 are shown in Figure 6.

384 As can be seen from the plot, the 3 datasets exhibit similar patterns in terms of seasonality: all
385 are enhanced in March-April and in summer, and show a decrease in May. However two major
386 differences can be noted.

387 First, CrIS standardized NH_3 columns are higher in winter (November, December, and January)
388 compared to the other dataset which can be also be seen in Figure 3. This could be attributed to
389 a higher number of outliers, given the larger standard deviation (shaded areas, Figure 6) and no
390 attempt to account for potential non-detects when concentrations fall below the instrument
391 detection limits. For these months, NH_3 levels are low and undetectable by satellite
392 observations (Figures 2 and 3) so these high values could be interpreted as observational noise.
393 The detection limit depends on the instrument characteristics and atmospheric state, with IASI

394 minimum detection limit of ~2-3 ppbv ($\sim 4\text{-}6 \cdot 10^{15}$ molecules.cm⁻²) [Clarisse et al., 2010] and CrIS
395 $\sim 0.5\text{-}1.0$ ppbv ($\sim 1\text{-}2 \cdot 10^{15}$ molecules.cm⁻²) [Shephard and Cady-Pereira, 2015; Kharol et. al.,
396 2018]. Note that values below detection limits have not been filtered out from the IASI dataset
397 whereas the quality flag was used to discard CrIS's retrievals associated with DOFS ≤ 0.1
398 (Section 2.2.2) favors larger observed columns. Consequently, the normalized seasonal cycle
399 amplitude derived from CrIS is weaker than the IASI one.

400 Second, the CHIMERE standardized NH₃ columns are enhanced in September 2014, which is not
401 supported by the observations. It has been recently shown that CHIMERE overestimated NH₃
402 emissions in autumn over Europe [Couvidat et al., 2018]. Generally, the amplitude of the
403 modelled seasonal cycle exceeds the measured ones, which could be explained by higher
404 concentrations measured in winter due to the observational noise and lower emissions. This is a
405 different finding than in Schiferl et al. (2016) since they restricted IASI high relative errors when
406 comparing to the GEOS-Chem model over the United-States, which inherently favors larger
407 columns and thus lead to weaken the observed seasonal cycle.

408 Over the whole period, the coefficient of determination (r^2) between the standardized monthly
409 mean NH₃ columns derived from IASI (CrIS), and the CHIMERE model is 0.58 (0.18) for the
410 annual cycles of 2014 and 2015 with low associated p-values of $1.5 \cdot 10^{-5}$ (0.06) reflecting the
411 significance level of the fits (not shown here). If we only consider months of high NH₃ in the
412 domain from March to August, the correlation between the observational datasets and the
413 model is rather good with r^2 values between IASI (CrIS) and CHIMERE of 0.29 (0.14) with
414 associated p-values of 0.07 (0.24), as shown in Figure 7. Since annual total emissions are the
415 same for the two years and simply disaggregated with a monthly profile in the model, the
416 correlations reveal that the seasonal cycle is likely to be reproduced by the model. In addition,
417 year-to-year variability can be seen in the model with lower concentrations in March 2015
418 compared to 2014 for instance, despite constant emissions in the 2-years simulation. This
419 interannual variability is likely to be attributed to meteorological conditions changes. However,
420 the values of the r^2 lower than 0.5 indicate that the CHIMERE model only reproduces at most
421 half of the observed monthly temporal NH₃ variabilities in the domain. Similar variabilities are
422 found between the observations and the model outputs since the coefficients of correlation of
423 the standard deviations are 0.4 and 0.6 between CHIMERE and IASI and CrIS, respectively.

424 3.2.2. Spatial variability of NH₃ in springtime

425 The IASI and CrIS regional maps have been compared to the CHIMERE model for the March-April
426 period in 2014 and 2015 to evaluate the model's capacity to reproduce the spatial distribution
427 of the episodic emissions from fertilizer spreading practices in springtime, as well as their inter-
428 annual variability. Satellite NH₃ measurements in springtime have been gridded at 0.15°x 0.15°

429 spatial resolution, and the associated CHIMERE maps have been computed following the
430 coincident criteria described in section 2.4 at the same spatial resolution (Figures 8 and 9).

431 First one can notice that the spatial distribution of NH_3 observed in springtime by both satellite
432 instruments are in good agreement, even though their overpass time is different (~4 hours
433 apart). This was already seen in the inter-annual variability agreement seen in Figure 4. In spring
434 2014, IASI and CrIS both reveal three main regions of enhanced NH_3 concentrations (North,
435 Champagne-Ardennes, and Brittany/Pays de la Loire region) already identified by the 10-years
436 and 5-years of IASI and CrIS observation maps (Boxes A, B, and C of Figures 2 and 3). In 2015,
437 concentrations of NH_3 in the northern part of the domain are higher than in 2014, as indicated
438 by both IASI and CrIS observations (Figure 9, upper panels). Overall, satellite observations are
439 able to capture similar spatial distributions of high NH_3 concentrations in springtime, and their
440 evolution in time.

441 In spring 2014, the CHIMERE model reproduces the high concentrations in the three regions of
442 the domain identified in Figures 2 and 3. Additional NH_3 hot spots in the southeastern part of
443 the domain including the Po Valley, Switzerland, and the wine region between Besancon and
444 Lyon (blue box in Figure 8) are indicated by the CHIMERE model. NH_3 emissions in this latter
445 region are comparable to average agricultural plains over France. Only dispersion conditions
446 related to wind speed and boundary layer height can explain high NH_3 concentrations over this
447 area.

448 In spring 2015, satellite observations and the CHIMERE model outputs exhibit very similar
449 patterns in term of high NH_3 distributions, with however higher NH_3 concentrations indicated by
450 the model in the southern part of the domain (blue box in Figure 9).

451 Finally, the (model - observations) differences between the standardized NH_3 column derived
452 from the satellite instruments in springtime 2014-2015 and the corresponding NH_3 columns
453 derived from the CHIMERE model are shown in Figure 2 of the supplement information. One
454 can see that very similar patterns are presented when comparing the model to independent
455 satellite observations from IASI and CrIS: the modelled NH_3 concentrations are systematically
456 lower for both years over Belgium and United Kingdom, and higher in the southern part of the
457 domain (green square, Figure S3) including the Pays de la Loire region (box C in Figures 2 and 3),
458 and in the southeastern part of the domain (over the North part of Switzerland and the Plateau
459 du Jura region - between Besancon and Lyon cities – blue box in Figure 8). Reasons of enhanced
460 NH_3 columns derived from the model in this latter region are not clear yet. An explanation could
461 be that the temporal distribution of the emissions is misrepresented in the model since the
462 modelled concentrations are enhanced in April whereas the two satellite observations are
463 enhanced earlier in March for both years. It is worth noting that there are no EMEP stations
464 measuring surface NH_3 concentrations in these regions. As for the Brittany/Pays de la Loire

465 region, it has already been shown that the LOTOS-EUROS atmospheric model [Schaap et al.,
466 2008] using similar chemistry schemes and NH₃ emissions shows higher columns each year in
467 this area [Van Damme et al., 2014b].

468 3.3. Comparisons of PM_{2.5} concentrations in IdF derived from the Airparif 469 network and CHIMERE for 2014 and 2015

470 To evaluate the model capacity to reproduce PM_{2.5} concentrations over the Parisian region,
471 comparisons between the Airparif measurements network and the CHIMERE outputs have been
472 performed for 2014 and 2015 (Figure 11). For those years, concentrations of PM_{2.5} are
473 measured hourly from the surface at 13 Airparif stations distributed over the IdF region (black
474 dots, Figure 1). To compare with the CHIMERE model, we have extracted the hourly surface
475 PM_{2.5} outputs in the IdF region, i. e. within a 50 km-radius circle from Paris.

476 Results of the comparison are shown in Figure 11. Day-to-Day variability of PM_{2.5} concentrations
477 at the surface is well represented by the CHIMERE model with however differences during
478 pollution events in March/April and in December for both years. The model may underestimate
479 PM_{2.5} concentrations in spring due to unknown PM_{2.5} formation processes, but overestimate
480 them in winter which could be due to uncertainties on NH₃ emissions from wood burning
481 processes. Overall, good agreement is found between the measurements and the model in term
482 of PM_{2.5} concentrations over the IdF region given values of r² of 0.56 (associated with p-value of
483 $6 \cdot 10^{-133}$), a slope of 0.67 ± 3.51 , with a slightly underestimation of the CHIMERE model given a
484 mean relative difference (calculated as model-observations/observations) of
485 -18% over 2014 and 2015.

486 3.4. Conditions for PM formation in the Paris megacity

487 To investigate the impact of intensive agriculture practices on the Paris megacity air quality, we
488 need to better understand the role of NH₃ in the formation of PM_{2.5} that depends, among
489 others, on specific meteorological conditions such as atmospheric temperature and humidity
490 that alter the gas-particle partitioning. The link between high NH₃ concentrations inducing PM_{2.5}
491 formation in the Paris megacity is known [Petetin et al., 2016; Zhang et al., 2013] but
492 quantification of such phenomena is difficult due the lack of long-term NH₃ monitoring in the
493 IdF region. PM_{2.5} is however measured hourly at several locations in Paris by the Airparif
494 network (<https://www.airparif.asso.fr/>, Figure 1). Thanks to the 10 years of IASI observations,
495 an observational evidence of PM_{2.5} formation in the IdF region (100 km around Paris - black box
496 in Figure 1) is represented in Figure S4. Simultaneous enhancements in March of PM_{2.5}
497 measured at the surface and NH₃ columns derived from the IASI observations over the IdF
498 region are clearly visible. However, high concentrations of NH₃ observed in summer are not
499 associated with high PM_{2.5} concentrations. This reflects the complexity of the PM_{2.5} formation

500 depending on various factors, such as NH₃ emissions, atmospheric chemistry (acidic content of
501 the atmosphere), transport, and specific meteorological conditions involved in the gas to solid
502 phase conversion between NH₃ and ammonium salts.

503 To evaluate the impact of long-range transport on NH₃ levels observed over the Parisian region
504 (IdF) in spring, back-trajectory analysis was performed. In total 231 24-hours back-trajectories
505 ending in Paris (period from February 15th to May 15th from 2013 to 2016) were classified into 8
506 clusters using HYSPLIT (<https://ready.arl.noaa.gov/HYSPLIT.php>). Figure 10 shows the mean
507 trajectories for each cluster associated with the average NH₃ total columns measured by IASI
508 over the IdF region. In this figure, higher NH₃ columns are found under the influence of air
509 masses transported from the northern part of the domain (over Belgium and the Netherlands,
510 clusters 4 and 5) and from the Brittany region (cluster 8), which are the major sources regions of
511 NH₃ in spring in the domain as previously identified (Figures 2 and 3). Indeed, NH₃ columns over
512 the Netherlands are relatively correlated to NH₃ columns measured over IdF since the cross-
513 correlation function is 0.37 at lag = 0 and above 0.3 at lag = ±1 day over the whole time period
514 (2008-2016 - Figure S5). Clusters 2 and 3 (Figure 10) are associated with intermediate NH₃ levels
515 since air masses moved slowly transporting NH₃-rich air from rural regions near IdF (such as the
516 Champagne-Ardennes region - Box A in Figures 2 and 3) to Paris. Finally, low NH₃ concentrations
517 are measured when air masses originated from ocean regions passing through continental areas
518 with minor NH₃ sources in spring (clusters 1, 6 and 7, Figure 10). This reflects the importance of
519 long-range transport in the NH₃ budget observed over the Paris megacity in spring.

520 To quantitatively assess the influence of meteorological parameters on the formation of PM_{2.5}
521 from NH₃ in the IdF region, timeseries of NH₃ total columns, PM_{2.5} surface concentrations, and
522 five meteorological parameters (temperature at 2 m, boundary layer height, total precipitation,
523 relative humidity, and wind field) derived from ECMWF - ERA-5 [Dee et al., 2011, Copernicus
524 Climate Change Service (C3S), 2017] were analyzed. To compute daily and monthly means, IASI
525 NH₃ total columns have been averaged over IdF (black box in Figure 1), PM_{2.5} concentrations
526 measured between 9 AM and 11 AM have been averaged over the 14 stations (dark points in
527 Figure 1), and ECMWF data have been averaged over a 300 km region around Paris (the blue
528 box in Figure 1). Figure 12 shows all these parameters for spring 2014.

529 We have flagged pollution episodes in both time series (PM_{2.5} and NH₃) by selecting data above
530 1-sigma standard deviation over the mean of the datasets from 2013 to 2016. This time period
531 was selected to have enough IASI observations in the IdF region. Then two cases have been
532 defined to study the temporal correlation between NH₃ and PM_{2.5}: case A in which both NH₃ and
533 PM_{2.5} pollution episodes appear simultaneously, i.e. within the same day or 2 days apart
534 (shaded in red in Figure 12); case B in which pollution episodes appear at least 3 days apart
535 (shaded in blue in Figure 12). In Figure 12, a strong relationship between peaks of NH₃, PM_{2.5}

536 and meteorological parameters can be seen. For example, between March 3rd and March 19th
537 2014 (case A), the boundary layer height is exceptionally low (456 m; compared to 760 m on
538 average); the temperature is relatively low (280 K; 282 K on average); and there is no
539 precipitation (0.01 mm/h; 0.11 mm/h on average). One note that peaks of maximum NH₃
540 observed in IdF on March 11th and 12th are associated with air masses coming from the northern
541 part of the domain (clusters 4 and 5 in Figure 10). In contrast, for the case B in which
542 appearance of peaks of NH₃ and PM_{2.5} is not simultaneous, meteorological conditions are
543 different: the boundary layer is thicker (908 m on April 23rd 2014), or temperature is higher (285
544 K on April 11th 2014).

545 To further investigate the influence of meteorological parameters on the pollution episodes in
546 the IdF region, detailed analysis have been made over the whole dataset. Figure 13 shows the
547 statistical distribution of meteorological parameters corresponding to case A, case B, and all
548 observations. One can see that for the whole dataset the boundary layer height is significantly
549 lower in case A (550 ± 205 m) than in case B (751 ± 276 m), and that precipitations are absent in
550 case A (0,019 mm/h) compared to case B (0,085 mm/h). The temperature at 2 meters also
551 differs between the two cases (case A: 278 ± 3 K; case B: 282 ± 4 K), but the humidity is almost
552 the same (70% ± 17% versus 75% ± 18). Results also suggest that simultaneous enhancements of
553 NH₃ and PM_{2.5} over Paris (cases A) are mainly associated with wind fields dominantly coming
554 from the Northeast part of the domain (Figure S6). Thus the combination of the following four
555 meteorological parameters favors simultaneous appearances of NH₃ and of PM_{2.5} in Paris (i.e.
556 case A): low surface temperatures (5°C), with thin boundary layers (~500m), rare precipitations,
557 and northeast wind.. In addition, the Wilcoxon-Mann-Whitney test ([Wilks, 2011], not shown
558 here) indicates that each single parameter has no significant influence on the NH₃-PM_{2.5}
559 correlation. Therefore only a combination of these different parameters has an impact on
560 secondary aerosol formation from NH₃.

561 An explanation of these findings might be that anticyclonic conditions (low planetary boundary
562 layer), preventing pollutant dispersions in the lower atmosphere [Salmond and McKendry,
563 2005], along with moderate wind fields allow NH₃ plumes to be transported from rural to urban
564 regions [Petit et al., 2015]. In addition, thanks to relatively low atmospheric temperatures and a
565 moderate relative humidity, conversion of gas phase NH₃ to ammonium salts is then
566 accentuated via optimal phase equilibrium [Watson et al., 1994; Nenes et al., 1998]. Finally,
567 with the absence of rain, ammonium salts are stabilized in the aerosols.

568 Our observations are in agreement with previous studies [Bessagnet et al., 2016; Wang et al.,
569 2015], which have shown that the formation of ammonium salt needs a specific humidity of 60 -
570 70%, mainly because it corresponds to the deliquescence point of NH₄NO₃ in ambient air. This is
571 in agreement with our results since the mean of relative humidity in case A is 70%. Our results

572 also support the idea that a relatively low atmospheric temperature favor $\text{PM}_{2.5}$ formation in
573 particular since the phase equilibrium leads to NH_4NO_3 decomposition above 30 °C.

574 4. Conclusions

575 This study focuses on seasonal and inter-annual variabilities of NH_3 concentrations in a 400 km
576 radius-circle area around Paris to assess the evolution of major NH_3 agricultural sources and its
577 key role in the formation of the secondary aerosols that affect air quality over the Paris
578 megacity.

579 Thanks to 10-years and 5-years of regional NH_3 observations derived from IASI and CrIS, three
580 main regions of high NH_3 occurring between March and August were identified. Observed inter-
581 annual variabilities of NH_3 concentrations have been discussed with respect to total
582 precipitations and atmospheric temperature, showing that total precipitations are anti-
583 correlated with high NH_3 concentrations, and that mild temperature in late winter might cause
584 precocious fertilizer spreading due to advanced phenological growth stage.

585 To evaluate our knowledge on agricultural emissions in terms of intensity and both spatial and
586 temporal distributions, coincident CHIMERE model outputs have been compared to satellite
587 observations of IASI and CrIS for 2014 and 2015. The annual cycle is well reproduced by the
588 model but it is only able to reproduce half of the observed atmospheric NH_3 variability. Focusing
589 on spring periods (March-April 2014 and 2015) of episodic NH_3 emissions, the two independent
590 satellite observations derived from IASI and CrIS show very similar spatial distributions of high
591 NH_3 concentrations, as well as their evolution in time. The comparison between CHIMERE NH_3
592 columns and coincident satellite observations highlights the same difference spatial patterns
593 with a systematic underestimation of NH_3 concentrations from the model over Belgium and an
594 overestimation in the southern part of the domain (French Brittany/Pays de la Loire and Plateau
595 du Jura regions, as well as North of Switzerland).

596 Focusing on the Ile-de-France (IdF, 100 km around Paris) region, we found that air masses
597 originated from rich- NH_3 areas, mainly the northern part of the domain over Belgium and the
598 Netherlands, increase the observed NH_3 total columns measured by IASI over the urban area of
599 Paris. In this region, we also found that the CHIMERE model is able to reproduce the day-to-day
600 variability of $\text{PM}_{2.5}$ concentrations (r^2 of 0.56), with however an underestimation during spring
601 pollution events, which could be due to unknown secondary aerosol formation processes.

602 To assess the link between NH_3 and $\text{PM}_{2.5}$ over the Parisian (IdF) region, the main
603 meteorological parameters driving the optimal conditions involved in the $\text{PM}_{2.5}$ formation have
604 been identified. The results show that relatively low temperature, thin boundary layer, coupled
605 with almost no precipitation and wind coming from the northeast, favor the $\text{PM}_{2.5}$ formation

606 with the presence of atmospheric NH₃ in the IdF region. Based on a more observational
607 approach over large time scale, this work is in agreement with previous studies.

608 This study highlights the need for a better representative NH₃ monitoring to improve numerical
609 simulation of spatial and temporal NH₃ variabilities, especially at fine scales. In order to
610 compare IASI and CrIS data in absolute values, it would be recommended to derive both
611 datasets using the same retrieval algorithm. Thus, by combining these datasets bi-daily NH₃
612 total columns in absolute values at regional scale would be provided. This would help inferring
613 variability of top-down NH₃ emissions. Complementarily, long term quantification of NH₃ diurnal
614 cycle inside Paris would improve comparisons with local PM_{2.5} needed to understand secondary
615 aerosols formations. For this purpose, an ongoing activity consists in the deployment of a mini-
616 DOAS instrument [Volten et al., 2012] used for long-term and continuous monitoring of
617 atmospheric NH₃ concentrations in the center of Paris from the QUALAIR platform
618 ([https://www.ipsl.fr/en/Our-research/Atmospheric-chemistry-and-air-quality/Tropospheric-
619 chemistry/QUALAIR](https://www.ipsl.fr/en/Our-research/Atmospheric-chemistry-and-air-quality/Tropospheric-chemistry/QUALAIR)). Finally, the geostationary-orbit sounder IRS-MTG ([Stuhlmann et al.,
620 2005], to be launched after 2022) will provide NH₃ columns at very high sampling rate (every 0.5
621 hour over Europe) with an unprecedented spatial resolution (pixel size of 4 km).

622
623 Author contribution:
624 CV wrote the paper with contributions of all coauthors. CV and CC designed the study. MV, LC,
625 and SW performed IASI retrievals and ED, MWS, and KEC performed the CrIS retrievals. FM ran
626 the CHIMERE simulations. CV and TW analyzed the data with guidance from CC and PFC. All
627 authors discussed the results and contributed to the final paper.

628 Acknowledgement:
629 IASI is a joint mission of Eumetsat and the Centre National d'Etudes Spatiales (CNES, France).
630 This work was supported by the CNES. It is based on observations with IASI embarked on
631 Metop. The IASI Level-1C data are distributed in near real time by Eumetsat through the
632 EumetCast system distribution. The authors acknowledge the AERIS data infrastructure
633 (<http://iasi.aeris-data.fr/NH3/>) for providing access to the IASI Level-1C data and Level-2 NH₃
634 data used in this study. The French scientists are grateful to CNES (TOSCA) and Centre National
635 de la Recherche Scientifique (CNRS) for financial support. The research in Belgium is also funded
636 by the Belgian State Federal Office for Scientific, Technical and Cultural Affairs and the European
637 Space Agency (ESA Prodex IASI Flow project). The CrIS Fast Physical Retrieval (CFPR) NH₃ data is
638 provide through a joint collaboration between Environment and Climate Change Canada (ECCC)
639 and Atmospheric and Environmental Research (AER), Inc. (USA). The Level 1 and Level 2 input
640 data for CFPR were obtained from the University of Wisconsin-Madison Space Science and
641 Engineering Center (SSEC) and the NOAA Comprehensive Large Array-Data Stewardship System
642 (CLASS) (Liu et al.,2014), with special thanks to Axel Graumann (NOAA).

643 References

- 644 Battye, W., Aneja, V. P., and Schlesinger W. H.: Is nitrogen the next carbon?, *Earth's Future*, 5,
645 894–904, doi:10.1002/2017EF000592, 2017.
- 646 Beer, R., Shephard, M. W., Kulawik, S. S., Clough, S. A., Eldering, A., Bowman, K. W., Sander, S.
647 P., Fisher, B. M., Payne, V. H., Luo, M., Osterman, G. B., and Worden, J. R.: First satellite
648 observations of lower tropospheric ammonia and methanol, *Geophys. Res. Lett.*, 35, L09801,
649 doi:10.1029/2008GL033642, 2008.
- 650 Behera, S. N., Sharma, M., Aneja, V. P., and Balasubramanian, R.: Ammonia in the atmosphere: a
651 review on emission sources, atmospheric chemistry and deposition on terrestrial bodies, *Environ.*
652 *Sci. Pollut. Res. Int.*, 20, 8092-8131, doi: 10.1007/s11356-013-2051-9, 2013.
- 653 Bessagnet, B., Meleux, F., Favez, O., Beauchamp, M., Colette, A., Couvidat, F., Rouil, L., Menut,
654 L. : Le rôle de l'agriculture sur les concentrations en particules dans l'atmosphère et l'apport de
655 la modélisation (the role of agriculture on the concentrations of particles in the atmosphere and
656 supply modeling), *Pollution atmosphérique, climat, santé, société*, 229–230, 154–165, 2016.
- 657 Bey, I., Jacob, D. J., Yantosca, R. M., Logan, J. A., Field, B., Fiore, A. M., Li, Q., Liu, H., Mickley, L.
658 J., and Schultz, M.: Global modeling of tropospheric chemistry with assimilated meteorology:
659 Model description and evaluation, *J. Geophys. Res.*, 106, 23,073-23,096, 2001.
- 660 Clerbaux, C., Boynard, A., Clarisse, L., George, M., Hadji-Lazaro, J., Herbin, H., Hurtmans, D.,
661 Pommier, M., Razavi, A., Turquety, S., Wespes, C., and Coheur, P.-F.: Monitoring of atmospheric
662 composition using the thermal infrared IASI/MetOp sounder, *Atmos. Chem. Phys.*, 9, 6041–
663 6054, doi:10.5194/acp-9-6041-2009,2009
- 664 CEIP, Centre on Emission Inventories and Projections, 'EMEP officially reported emission data',
665 http://www.ceip.at/ms/ceip_home1/ceip_home/webdab_emepdatabase/reported_emissiondata/,
666 last access July 2018.
- 667 CITEPA, Centre Interprofessionnel Technique d'Etudes de la Pollution Atmosphérique, Format
668 SECTEN, <https://www.citepa.org/fr/air-et-climat/polluants/aep-item/ammoniac>, last access
669 April 2018.
- 670 Clarisse, L., Clerbaux, C., Dentener, F., Hurtmans, D., and Coheur, P.-F.: Global ammonia
671 distribution derived from infrared satellite observations, *Nat. Geosci.*, 2, 479–483,
672 <https://doi.org/10.1038/ngeo551>, 2009.
- 673 Clarisse, L., Shephard, M., Dentener, F., Hurtmans, D., Cady-Pereira, K., Karagulian, F., Van
674 Damme, M., Clerbaux, C., and Coheur, P.-F.: Satellite monitoring of ammonia: A case study of

675 the San Joaquin Valley, *J. Geophys. Res.*, 115, D13302, <https://doi.org/10.1029/2009JD013291>,
676 2010.

677 Copernicus Climate Change Service (C3S): ERA5: Fifth generation of ECMWF atmospheric
678 reanalyses of the global climate . Copernicus Climate Change Service Climate Data Store (CDS),
679 date of access. <https://cds.climate.copernicus.eu/cdsapp#!/home>, 2017.

680 Couvidat, F., Bessagnet, B., Garcia-Vivanco, M., Real, E., Menut, L., and Colette, A.: Development
681 of an inorganic and organic aerosol model (CHIMERE 2017 β v1.0): seasonal and spatial
682 evaluation over Europe, *Geosci. Model Dev.*, 11, 165-194, [https://doi.org/10.5194/gmd-11-165-](https://doi.org/10.5194/gmd-11-165-2018)
683 2018, 2018.

684 Corso, M. Medina, S., and Tillier, C. : Quelle est la part des pics de pollution dans les effets à
685 court terme de la pollution de l'air sur la santé dans les villes de France ? Saint-Maurice: Santé
686 publique France, ISBN : 979-10-289-0259-9, 2016.

687 Dammers, E., Palm, M., Van Damme, M., Vigouroux, C., Smale, D., Conway, S., Toon, G. C.,
688 Jones, N., Nussbaumer, E., Warneke, T., Petri, C., Clarisse, L., Clerbaux, C., Hermans, C., Lutsch,
689 E., Strong, K., Hannigan, J. W., Nakajima, H., Morino, I., Herrera, B., Stremme, W., Grutter, M.,
690 Schaap, M., Wichink Kruit, R. J., Notholt, J., Coheur, P.-F., and Erisman, J. W.: An evaluation of
691 IASI-NH₃ with ground-based Fourier transform infrared spectroscopy measurements, *Atmos.*
692 *Chem. Phys.*, 16, 10351–10368, <https://doi.org/10.5194/acp-16-10351-2016>, 2016.

693 Dammers, E., Shephard, M. W., Palm, M., Cady-Pereira, K., Capps, S., Lutsch, E., Strong, K.,
694 Hannigan, J. W., Ortega, I., Toon, G. C., Stremme, W., Grutter, M., Jones, N., Smale, D., Siemons,
695 J., Hrpcek, K., Tremblay, D., Schaap, M., Notholt, J., and Erisman, J. W.: Validation of the CrIS fast
696 physical NH₃ retrieval with ground-based FTIR, *Atmos Meas Tech*, 10, 2645-2667, [10.5194/amt-](https://doi.org/10.5194/amt-10-2645-2017)
697 10-2645-2017, 2017.

698 Dee, D. P., Uppala, S. M., Simmons, A. J., Berrisford, P., Poli, P., Kobayashi, S., Andrae, U.,
699 Balmaseda, M. A., Balsamo, G., Bauer, P., Bechtold, P., Beljaars, A. C. M., van de Berg, L., Bidlot,
700 J., Bormann, N., Delsol, C., Dragani, R., Fuentes, M., Geer, A. J., Haimberger, L., Healy, S. B.,
701 Hersbach, H., Hólm, E. V., Isaksen, L., Kållberg, P., Köhler, M., Matricardi, M., McNally, A. P.,
702 Monge-Sanz, B. M., Morcrette, J.-J., Park, B.-K., Peubey, C., de Rosnay, P., Tavolato, C., Thépaut,
703 J.-N. and Vitart, F.: The ERA-Interim reanalysis: configuration and performance of the data
704 assimilation system. *Q.J.R. Meteorol. Soc.*, 137: 553–597. doi: 10.1002/qj.828, 2011.

705 Erisman, J. W., Sutton, M. A., Galloway, J. N., Klimont, Z., and Winiwarter, W.: How a century of
706 ammonia synthesis changed the world, *Nat. Geosci.*, 1, 636–639, doi:10.1038/ngeo325, 2008.

707 Fortems-Cheiney, A., Dufour, G., Hamaoui-Laguel, L., Foret, G., Siour, G., Van Damme, M.,
708 Meleux, F., Coheur, P.-F., Clerbaux, C., Clarisse, L., Favez, O., Wallasch, M., and Beekmann, M.:

709 Unaccounted variability in NH₃ agricultural sources detected by IASI contributing to European
710 spring haze episode, *Geophys. Res. Lett.*, 43, 5475–5482, doi:10.1002/2016GL069361, 2016.

711 Fuzzi, S., Baltensperger, U., Carslaw, K., Decesari, S., Denier van der Gon, H., Facchini, M. C.,
712 Fowler, D., Koren, I., Langford, B., Lohmann, U., Nemitz, E., Pandis, S., Riipinen, I., Rudich, Y.,
713 Schaap, M., Slowik, J. G., Spracklen, D. V., Vignati, E., Wild, M., Williams, M., and Gilardoni, S.:
714 Particulate matter, air quality and climate: lessons learned and future needs, *Atmos. Chem.*
715 *Phys.*, 15, 8217-8299, <https://doi.org/10.5194/acp-15-8217-2015>, 2015.

716 Galloway, J. N., Aber, J. D., Erisman, J. W., Seitzinger, S. P., Howarth, R. W., Cowling, E. B., and
717 Cosby, B. J.: The Nitrogen Cascade, *BioScience*, 53, doi: 10.1641/0006-3568(2003), 2003.

718 Gong, L., Lewicki, R., Griffin, R. J., Tittel, F.K., Lonsdale, C. R., Stevens, R. G., Pierce, J. R., Malloy,
719 Q. G. J., Travis, S. A., Bobmanuel, L. M., Lefer, B. L., and Flynn, J. H.: Role of atmospheric
720 ammonia in particulate matter formation in Houston during summertime, *Atmos. Environ.*, 77:
721 893–900, <https://doi.org/10.1016/j.atmosenv.2013.04.079>, 2013.

722 Hamaoui-Laguel, L., Meleux, F., Beekmann, M., Bessagnet, B., Générumont, S., Cellier, P.,
723 Létinois, L.: Improving ammonia emissions in air quality modelling for France, *Atmos. Environ.*,
724 92, 584–595, doi:10.1016/j.atmosenv.2012.08.002, 2014.

725 Heald, C. L., Collett Jr., J. L., Lee, T., Benedict, K. B., Schwandner, F. M., Li, Y., Clarisse, L.,
726 Hurtmans, D. R., Van Damme, M., Clerbaux, C., Coheur, P.-F., Philip, S., Martin, R. V., and Pye, H.
727 O. T.: Atmospheric ammonia and particulate inorganic nitrogen over the United States, *Atmos.*
728 *Chem. Phys.*, 12, 10295–10312, doi:10.5194/acp-12-10295-2012, 2012.

729 Hernández, D. L., Vallano, D. M., Zavaleta, E. S., Tzankova, Z., Pasari, J. R., Weiss, S., Selmants, P.
730 C., and Morozumi, C.: Nitrogen Pollution Is Linked to US Listed Species Declines, *BioScience*, 66
731 (3), 213–222, <https://doi.org/10.1093/biosci/biw003>, 2016.

732 Holland, E. A., Bertman, S. B., Carroll, M. A., Guenther, A. B., Shepson, P. B., Sparks, J. P., and
733 Lee-Taylor, J.: U.S. Nitrogen Science Plan Focuses Collaborative Efforts, *Eos. Trans. Am. Geophys.*
734 *Union.*, 86(27), 253-260, 2005.

735 Isbell F., Reich, P. B., Tilman, D., Hobbie, S. E., Polasky, S., and Binder S.: Nutrient enrichment,
736 biodiversity loss, and consequent declines in ecosystem productivity, *PNAS*, 110 (29), 11911-
737 11916, <https://doi.org/10.1073/pnas.1310880110>, 2013.

738 Kaiser, J. W., Heil, A., Andreae, M. O., Benedetti, A., Chubarova, N., Jones, L., Morcrette, J.-J.,
739 Razinger, M., Schultz, M. G., Suttie, M., and van der Werf, G. R.: Biomass burning emissions
740 estimated with a global fire assimilation system based on observed fire radiative power. *BG*,
741 9:527-554, 2012.

742 Kharol, S. K., M. W. Shephard, C. A. McLinden, L. Zhang, C. E. Sioris, J. M. O'Brien, R. Vet, K. E.
743 Cady-Pereira, E. Hare, J. Siemons, and N. A. Krotkov.: Dry deposition of reactive nitrogen from
744 satellite observations of ammonia and nitrogen dioxide over North America, *Geophysical*
745 *Research. Letters*, 45, 1157-1166, <https://doi.org/10.1002/2017GL075832>, 2018.

746

747 Kranenburg, R., Hendriks, C., Kuenen, J., and Schaap, M.: Improved Modelling of Ammonia by
748 Using Manure Transport Data, In *International Technical Meeting on Air Pollution Modelling and*
749 *its Application* (pp. 483-486). Springer, Cham, December 2016.

750

751 Kuenen, J. J. P., Visschedijk, A. J. H., Jozwicka, M., and Denier van der Gon, H. A. C.: TNO-
752 MACC_II emission inventory; a multi-year (2003–2009) consistent high-resolution European
753 emission inventory for air quality modelling, *Atmos. Chem. Phys.*, 14, 10963-10976,
754 <https://doi.org/10.5194/acp-14-10963-2014>, 2014.

755

756 Li, Y., Thompson, T. M., Van Damme, M., Chen, X., Benedict, K. B., Shao, Y., Day, D., Boris, A.,
757 Sullivan, A. P., Ham, J., Whitburn, S., Clarisse, L., Coheur, P.-F., and Collett Jr., J. L.: Temporal and
758 spatial variability of ammonia in urban and agricultural regions of northern Colorado, United
759 States, *Atmos. Chem. Phys.*, 17, 6197-6213, <https://doi.org/10.5194/acp-17-6197-2017>, 2017.

760

761 Mailler, S., Menut, L., Khvorostyanov, D., Valari, M., Couvidat, F., Siour, G., Turquety, S., Briant,
762 R., Tuccella, P., Bessagnet, B., Colette, A., Letinois, L., and Meleux, F.: CHIMERE-2017: from
763 urban to hemispheric chemistry-transport modeling, *Geosci. Model Dev.*, 10, 2397-2423,
764 <https://doi.org/10.5194/gmd-10-2397-2017>, 2017.

765

765 Menut, L., Bessagnet, B., Khvorostyanov, D., Beekmann, M., Blond, N., Colette, A., Coll, I., Curci,
766 G., Foret, G., Hodzic, A., Mailler, S., Meleux, F., Monge, J.L., Pison, I., Siour, G., Turquety, S.,
767 Valari, M., Vautard, R., and Vivanco, M.G.: CHIMERE 2013: a model for regional atmospheric
768 composition modelling, *Geosci. Model Dev*, 6, 981-1028, doi:10.5194/gmd-6-981-2013, 2013.

769

769 Moran, M. D., Dastoor, A., and Morneau, G.: Long-Range Transport of Air Pollutants and
770 Regional and Global Air Quality Modelling. In: Taylor E., McMillan A. (eds) *Air Quality*
771 *Management*, Springer, Dordrecht, 2014.

772

772 Moncet, J.-L., Uymin G., Lipton A. E., and Snell H. E.: Infrared radiance modeling by optimal
773 spectral sampling, *J. Atmos. Sci.*, 65, 3917-3934, <https://doi.org/10.1175/2008JAS2711.1>, 2008.

774

774 Myhre, G., Samset, B. H., Schulz, M., Balkanski, Y., Bauer, S., Berntsen, T. K., Bian, H., Bellouin,
775 N., Chin, M., Diehl, T., Easter, R. C., Feichter, J., Ghan, S. J., Hauglustaine, D., Iversen, T., Kinne,
776 S., Kirkevåg, A., Lamarque, J.-F., Lin, G., Liu, X., Lund, M. T., Luo, G., Ma, X., van Noije, T., Penner,
777 J. E., Rasch, P. J., Ruiz, A., Seland, Ø., Skeie, R. B., Stier, P., Takemura, T., Tsigaridis, K., Wang, P.,

778 Wang, Z., Xu, L., Yu, H., Yu, F., Yoon, J.-H., Zhang, K., Zhang, H., and Zhou, C.: Radiative forcing of
779 the direct aerosol effect from AeroCom Phase II simulations, *Atmos. Chem. Phys.*, 13, 1853-
780 1877, <https://doi.org/10.5194/acp-13-1853-2013>, 2013.

781 Nenes, A.; Pandis, S. N.; Pilinis, C.: ISORROPIA: A New Thermodynamic Equilibrium Model for
782 Multiphase Multicomponent Inorganic Aerosols. *Aquat. Geoch.*, 4, 123-152, 1998.

783 National Emission Ceilings Directive (NEC) reporting status, doi:10.2800/984979,
784 [https://www.eea.europa.eu/themes/air/national-emission-ceilings/nec-directive-reporting-](https://www.eea.europa.eu/themes/air/national-emission-ceilings/nec-directive-reporting-status-2018)
785 [status-2018](https://www.eea.europa.eu/themes/air/national-emission-ceilings/nec-directive-reporting-status-2018), 2018.

786 Nenes, A.; Pandis, S. N.; Pilinis, C.: ISORROPIA: A New Thermodynamic Equilibrium Model for
787 Multiphase Multicomponent Inorganic Aerosols. *Aquat. Geoch.*, 4, 123-152, 1998.

788 Nowak, J. B., Neuman, J. A., Bahreini, R., Middlebrook, A. M., Holloway, J. S., McKeen, S. A.,
789 Parrish, D. D., Ryerson, T. B., and Trainer, M.: Ammonia sources in the California South Coast Air
790 Basin and their impact on ammonium nitrate formation, *Geophys. Res. Lett.*, 39, L07804,
791 <https://doi.org/10.1029/2012GL051197>, 2012.

792 Petetin, H., Sciare, J., Bressi, M., Gros, V., Rosso, A., Sanchez, O., Sarda-Estève, R., Petit, J.-E.,
793 and Beekmann, M.: Assessing the ammonium nitrate formation regime in the Paris megacity
794 and its representation in the CHIMERE model, *Atmos. Chem. Phys.*, 16, 10419-10440,
795 <https://doi.org/10.5194/acp-16-10419-2016>, 2016.

796 Petit, J.-E., Favez, O., Sciare, J., Crenn, V., Sarda-Estève, R., Bonnaire, N., Močnik, G., Dupont, J.-
797 C., Haeffelin, M., and Leoz-Garziandia, E.: Two years of near real-time chemical composition of
798 submicron aerosols in the region of Paris using an Aerosol Chemical Speciation Monitor (ACSM)
799 and a multi-wavelength Aethalometer, *Atmos. Chem. Phys.*, 15, 2985-3005,
800 <https://doi.org/10.5194/acp-15-2985-2015>, 2015.

801 Petit, J.-E., Amodeo, T., Meleux, F., Bessagnet, B., Menut, L., Grenier, D., Pellan, Y., Ockler, A.,
802 Rocq, B., Gros, V., Sciare, J., and Favez, O.: Characterising an intense PM pollution episode in
803 March 2015 in France from multi-site approach and near real time data: Climatology,
804 variabilities, geographical origins and model evaluation, *Atmospheric Environment*, Volume 155,
805 <https://doi.org/10.1016/j.atmosenv.2017.02.012>, 2017.

806 Pinder, R. W., Adams, P. J., Pandis, S.N., and Gilliland, A. B.: Temporally resolved ammonia
807 emission inventories: current estimates, evaluation tools, and measurement needs, *J. Geophys.*
808 *Res.*, 111, D16310, <http://dx.doi.org/10.1029/2005JD006603>, 2006.

809 Pope III, C. A., Ezzati M., and Dockery, D. W.: Fine-particulate air pollution and life expectancy in
810 the United States, *New England J. Med.*, 360 (4), 376-386, 2009.

811 Ramanantenasoa, M. M. J., Gilliot, J.-M., Mignolet, C., Bedos, C., Mathias, E., Eglin, T.,
812 Makowski, D., and Générumont, S.: A new framework to estimate spatio-temporal ammonia
813 emissions due to nitrogen fertilization in France, *Science of The Total Environment*, 645, 205 –
814 219, <https://doi.org/10.1016/j.scitotenv.2018.06.202>, 2018.

815 Robinson, T. P, Wint, G. R. W., Conchedda, G., Van Boeckel, T. P., Ercoli, V., Palamara, E., Cinardi,
816 G., D’Aielli, L., Hay, S., and Gilbert, M.: Mapping the global distribution of livestock, *PLoS One*,
817 9(5): e96084, <https://doi.org/10.1371/journal.pone.0096084>, 2014.

818 Rockström, J., Steffen, W., Noone, K., Persson, A., Chapin Iii, F. S., Lambin, E. F., Lenton, T. M.,
819 Scheffer, M., Folke, C., Schellnhuber, H. J., Nykvist, B., de Wit, C. A., Hughes, T., van der Leeuw,
820 S., Rodhe, H., Sörlin, S., Snyder, P. K., Costanza, R., Svedin, U., Falkenmark, M., Karlberg, L.,
821 Corell, R. W., Fabry, V. J., Hansen, J., Walker, B., Liverman, D., Richardson, K., Crutzen, P., and
822 Foley, J. A.: Planetary boundaries: Exploring the safe operating space for humanity, *Ecology and*
823 *Society*, 14, 2009.

824 Rodgers, C. D.: *Inverse Methods for Atmospheric Sounding: Theory and Practice*, vol. 2 of Series
825 on Atmospheric, Oceanic and Planetary Physics, edited by: Taylor, F. W., World Scientific, 2000.

826 Salmond, J. A., and McKendry, I. G.: A Review of Turbulence in the Very Stable Nocturnal
827 Boundary Layer and Its Implications for Air Quality, *Progress in Physical Geography*, 29 (2), 171–
828 188, 2005.

829 Scarlat, N., Fahl, F., Dallemand, J.-F., Monforti, F., and Motola, V.: A spatial analysis of biogas
830 potential from manure in Europe. *Renew. Sustain. Energy Rev.*, 94, 915–930,
831 <https://doi.org/10.1016/j.rser.2018.06.035>, 2018.

832 Schaap, M., Timmermans, R., Roemer, M., Boersen, G., Bultjes, P., Sauter, F., Velders, G., and
833 Beck, J.: The LOTOS-EUROS model: Description, validation and latest developments, *Int. J.*
834 *Environ. Pollut.*, 32, 270–290, doi:[10.1504/IJEP.2008.017106](https://doi.org/10.1504/IJEP.2008.017106), 2008.

835 Schiferl, Luke D., Heald, Colette L., van Damme, Martin, Clarisse, Lieven, Clerbaux, Cathy et al.
836 Interannual variability of ammonia concentrations over the United States: sources and
837 implications. *Atmospheric Chemistry and Physics*, 16 (18), 12305-12328, 2016.

838 Shephard, M.W., and Cady-Pereira, K.E.: Cross-track Infrared Sounder (CrIS) satellite
839 observations of tropospheric ammonia, *Atmos. Meas. Tech.*, 8, 1323-1336, 2015.

840 Shephard, M. W., Cady-Pereira, K. E., Luo, M., Henze, D. K., Pinder, R. W., Walker, J. T., Rinsland,
841 C. P., Bash, J. O., Zhu, L., Payne, V. H., and Clarisse, L.: TES ammonia retrieval strategy and global
842 observations of the spatial and seasonal variability of ammonia, *Atmos. Chem. Phys.*, 11, 10743–
843 10763, doi:10.5194/acp-11-10743-2011, 2011.

844 Skjøth, C. A., Geels, C., Berge, H., Gyldenkerne, S., Fagerli, H., Ellermann, T., Frohn, L. M.,
845 Christensen, J., Hansen, K. M., Hansen, K., and Hertel, O.: Spatial and temporal variations in
846 ammonia emissions – a freely accessible model code for Europe, *Atmos. Chem. Phys.*, **11**, 5221-
847 5236, <https://doi.org/10.5194/acp-11-5221-2011>, 2011.

848 Skyllakou, K., Murphy, B. N., Megaritis, A. G., Fountoukis, C., and Pandis, S. N.: Contributions of
849 local and regional sources to fine PM in the megacity of Paris, *Atmos. Chem. Phys.*, **14**, 2343-
850 2352, <https://doi.org/10.5194/acp-14-2343-2014>, 2014.

851 Sutton, M. A., Bleeker, A., Howard, C., Bekunda, M., Grizzetti, B., de Vries, W., van Grinsven, H.,
852 Abrol, Y., Adhya, T., Billen, G. and Davidson, E., Datta, A., Diaz, R., Erisman, J., Liu, X., Oenema,
853 O., Palm, C., Raghuram, N., Reis, S., Scholz, R., Sims, T., Westhoek, H., Zhang, F., with
854 contributions from Ayyappan, S., Bouwman, A., Bustamante, M., Fowler, D., Galloway, J., Gavito,
855 M., Garnier, J., Greenwood, S., Hellums, D., Holland, M., Hoysall, C., Jaramillo, V., Klimont, Z.,
856 Ometto, J., Pathak, H., Ploq Fichelet, V., Powlson, D., Ramakrishna, K., Roy, A., Sanders, K.,
857 Sharma, C., Singh, B., Singh, U., Yan, X., and Zhang, Y.: Our Nutrient World: The challenge to
858 produce more food and energy with less pollution. Global Overview of Nutrient Management,
859 Centre for Ecology & Hydrology on behalf of the Global Partnership on Nutrient Management
860 and the International Nitrogen Initiative, 114 pp., 2013.

861 Stuhlmann, R., Rodriguez, A., Tjemkes, S., Grandell, J., Arriaga, A., Bézy, J.-L., Aminou, D., and
862 Bensi, P.: Plans for EUMETSAT's Third Generation Meteosat (MTG) Geostationary Satellite
863 Program, *Adv. Space Res.*, **36**, 975–981, 2005.

864 Toro, R.A., Canales, M., Flocchini, R.G., Morales, R.G.E., and Leiva G, M.A.: Urban atmospheric
865 ammonia in Santiago City, Chile, *Aerosol Air Qual. Res.*, **14**: 33–44, doi:
866 10.4209/aaqr.2012.07.0189, 2014.

867 Van Damme, M., Clarisse, L., Heald, C. L., Hurtmans, D., Ngadi, Y., Clerbaux, C., Dolman, A. J.,
868 Erisman, J. W., and Coheur, P. F.: Global distributions, time series and error characterization of
869 atmospheric ammonia (NH₃) from IASI satellite observations, *Atmos. Chem. Phys.*, **14**, 2905–
870 2922, <https://doi.org/10.5194/acp-14-2905-2014>, 2014a.

871 Van Damme, M., Wichink Kruit, R. J., Schaap, M., Clarisse, L., Clerbaux, C., Coheur, P.-F.,
872 Dammers, E., Dolman, A. J., and Erisman, J. W.: Evaluating four years of atmospheric ammonia
873 (NH₃) over Europe using IASI satellite observations and LOTOS-EUROS model results, *J. Geophys.*
874 *Res.-Atmos.*, **119**, 9549-9566, 2014b.

875 Van Damme, M., Erisman, J. W., Clarisse, L., Dammers, E., Whitburn, S., Clerbaux, C., Dolman, A.
876 J., and Coheur, P.-F.: Worldwide spatiotemporal atmospheric ammonia (NH₃) columns variability
877 revealed by satellite, *Geophys. Res. Lett.*, **42** (20), 8660-8668, 2015a.

878 Van Damme, M., Clarisse, L., Dammers, E., Liu, X., Nowak, J. B., Clerbaux, C., Flechard, C. R.,
879 Galy-Lacaux, C., Xu, W., Neuman, J. A., Tang, Y. S., Sutton, M. A., Erisman, J. W., and Coheur, P.
880 F.: Towards validation of ammonia (NH_3) measurements from the IASI satellite, *Atmos. Meas.*
881 *Tech.*, 8, 1575-1591, <https://doi.org/10.5194/amt-8-1575-2015>, 2015b.

882 Van Damme, M., Whitburn, S., Clarisse, L., Clerbaux, C., Hurtmans, D., and Coheur, P.-F.: Version
883 2 of the IASI NH_3 neural network retrieval algorithm: near-real-time and reanalysed datasets,
884 *Atmos. Meas. Tech.*, 10, 4905-4914, <https://doi.org/10.5194/amt-10-4905-2017>, 2017.

885 Van Damme, M., Clarisse, L., Whitburn, S., Hadji-Lazaro J., Hurtmans, D., Clerbaux, C., and
886 Coheur, P.-F.: Industrial and agricultural ammonia point sources exposed, *Nature*, 564 (7734):
887 99, DOI: 10.1038/s41586-018-0747-1, 2018.

888 van Vuuren, D. P., Edmonds, J., Kainuma, M. et al. he Representative Concentration Pathways:
889 An overview, *Clim. Change*, 109 (1–2), 5–31, <https://doi.org/10.1007/s10584-011-0148-z>, 2011.

890 Volten, H., Bergwerff, J. B., Haaima, M., Lolkema, D. E., Berkhout, A. J. C., van der Hoff, G. R.,
891 Potma, C. J. M., Wichink Kruit, R. J., van Pul, W. A. J., and Swart, D. P. J.: Two instruments based
892 on differential optical absorption spectroscopy (DOAS) to measure accurate ammonia
893 concentrations in the atmosphere, *Atmos. Meas. Tech.*, 5, 413-427,
894 <https://doi.org/10.5194/amt-5-413-2012>, 2012.

895 Wang, S., Nan, J., Shi, C., Fu, Q., Gao, G., Wang, D., Cui, H., Saiz-Lopez A., and Zhou, B.:
896 Atmospheric ammonia and its impacts on regional air quality over the megacity of Shanghai,
897 China, *Scientific Reports*, 5, 15842, <http://dx.doi.org/10.1038/srep15842>, 2015.

898 Warner, J. X., Dickerson, R. R., Wei, Z., Strow, L. L., Wang, Y., and Liang, Q.: Increased
899 atmospheric ammonia over the world's major agricultural areas detected from space, *Geophys.*
900 *Res. Lett.*, doi: 10.1002/2016gl072305, 2017.

901 Warner, J. X., Wei, Z., Strow, L. L., Dickerson, R. R., and Nowak, J. B.: The global tropospheric
902 ammonia distribution as seen in the 13-year AIRS measurement record, *Atmos. Chem. Phys.*, 16,
903 5467-5479, <https://doi.org/10.5194/acp-16-5467-2016>, 2016.

904 Watson, J. G., Chow, J. C., Lurmann, F. W., and Musarra, S. P.: Ammonium Nitrate, Nitric Acid,
905 and Ammonia Equilibrium in Wintertime Phoenix, Arizona. *Air & Waste*, 44 (4), 405–412, 1994.

906 Wesely, M.: Parameterization of Surface Resistances to Gaseous Dry Deposition in Regional-
907 Scale Numerical Models. *Atmospheric Environment*, 23(23):1293–1304, 1989.

908 Whitburn, S., Van Damme, M., Clarisse, L., Bauduin, S., Heald, C., Hadji-Lazaro, J., Hurtmans, D.,
909 Zondlo, M., Clerbaux, C., and Coheur, P.-F.: A flexible and robust neural network IASI- NH_3

910 retrieval algorithm, *J. Geophys. Res. Atmos.*, 121, 6581–6599,
911 <https://doi.org/10.1002/2016JD024828>, 2016.

912 Wilks, Daniel S.: *Statistical Methods in the Atmospheric Sciences*, 3rd ed. Oxford, Waltham, MA:
913 Academic Press, 2011.

914 Ye, X., Ma, Z., Zhang, J., Du, H., Chen, J., Chen, H., Yang, X., Gao, W. and Geng, F.: Important role
915 of ammonia on haze formation in Shanghai, *Environ. Res. Lett.*, 6: 024019, doi:10.1088/1748-
916 9326/6/2/024019, 2011.

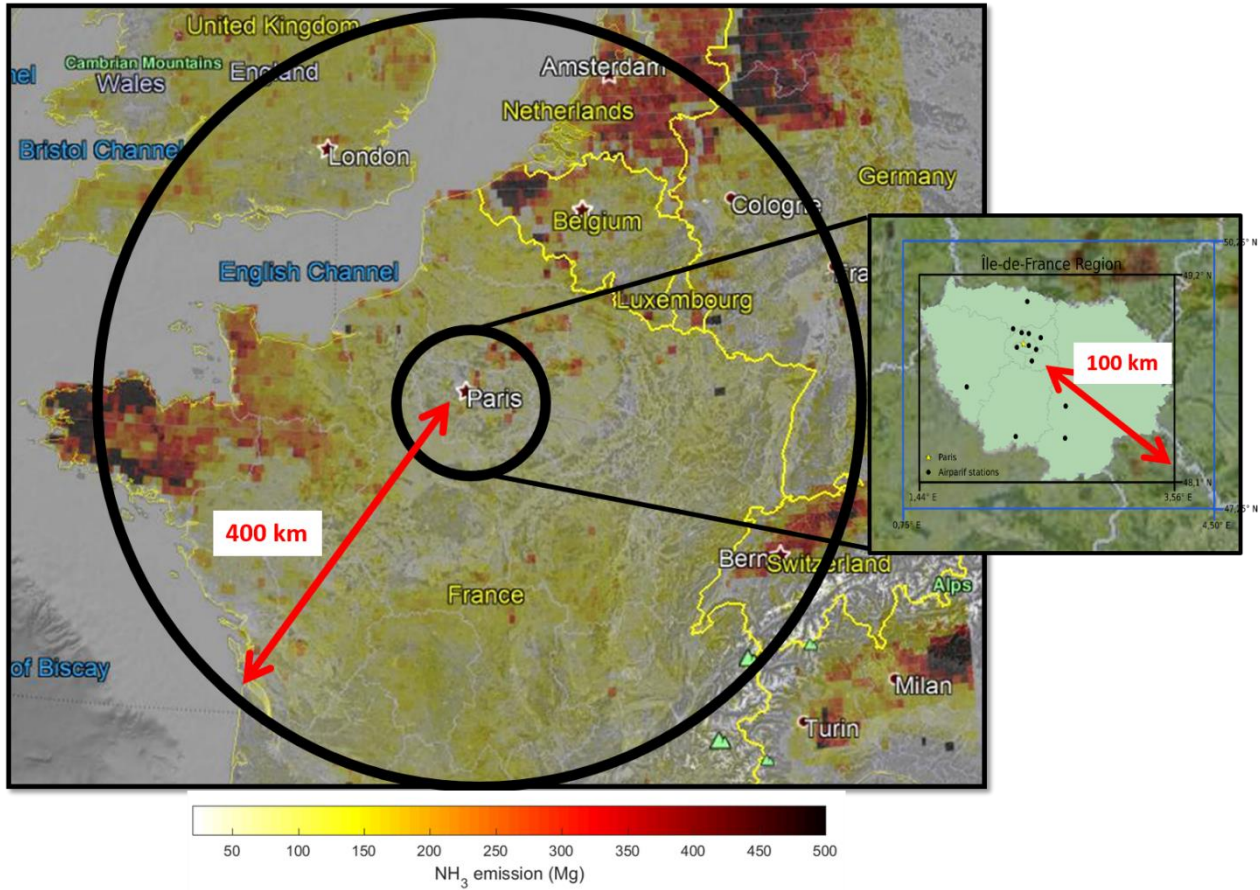
917 Zavyalov, V., Esplin, M., Scott, D., Esplin, B., Bingham, G., Hoffman, E., Lietzke, C., Predina, J.,
918 Frain, R., Suwinski, L., Han, Y., Major, C., Graham, B., and Phillips, L.: Noise performance of the
919 CrIS instrument, *J. Geophys. Res.*, doi: 10.1002/2013JD020457, 2013.

920 Zhang, Q. J., Beekmann, M., Drewnick, F., Freutel, F., Schneider, J., Crippa, M., Prevot, A. S. H.,
921 Baltensperger, U., Poulain, L., Wiedensohler, A., Sciare, J., Gros, V., Borbon, A., Colomb, A.,
922 Michoud, V., Doussin, J.-F., Denier van der Gon, H. A. C., Haeffelin, M., Dupont, J.-C., Siour, G.,
923 Petetin, H., Bessagnet, B., Pandis, S. N., Hodzic, A., Sanchez, O., Honoré, C., and Perrussel, O.:
924 Formation of organic aerosol in the Paris region during the MEGAPOLI summer campaign:
925 evaluation of the volatility-basis-set approach within the CHIMERE model, *Atmos. Chem. Phys.*,
926 13, 5767-5790, <https://doi.org/10.5194/acp-13-5767-2013>, 2013.

927 Zhao, M., Wang, S., Tan, J., Hua, Y., Wu, D., and Hao, J.: Variation of urban atmospheric
928 ammonia pollution and its relation with PM_{2.5} chemical property in winter of Beijing, China,
929 *Aerosol Air Qual. Res.*, 16, 1378–1389, <https://doi.org/10.4209/aaqr.2015.12.0699>, 2016.

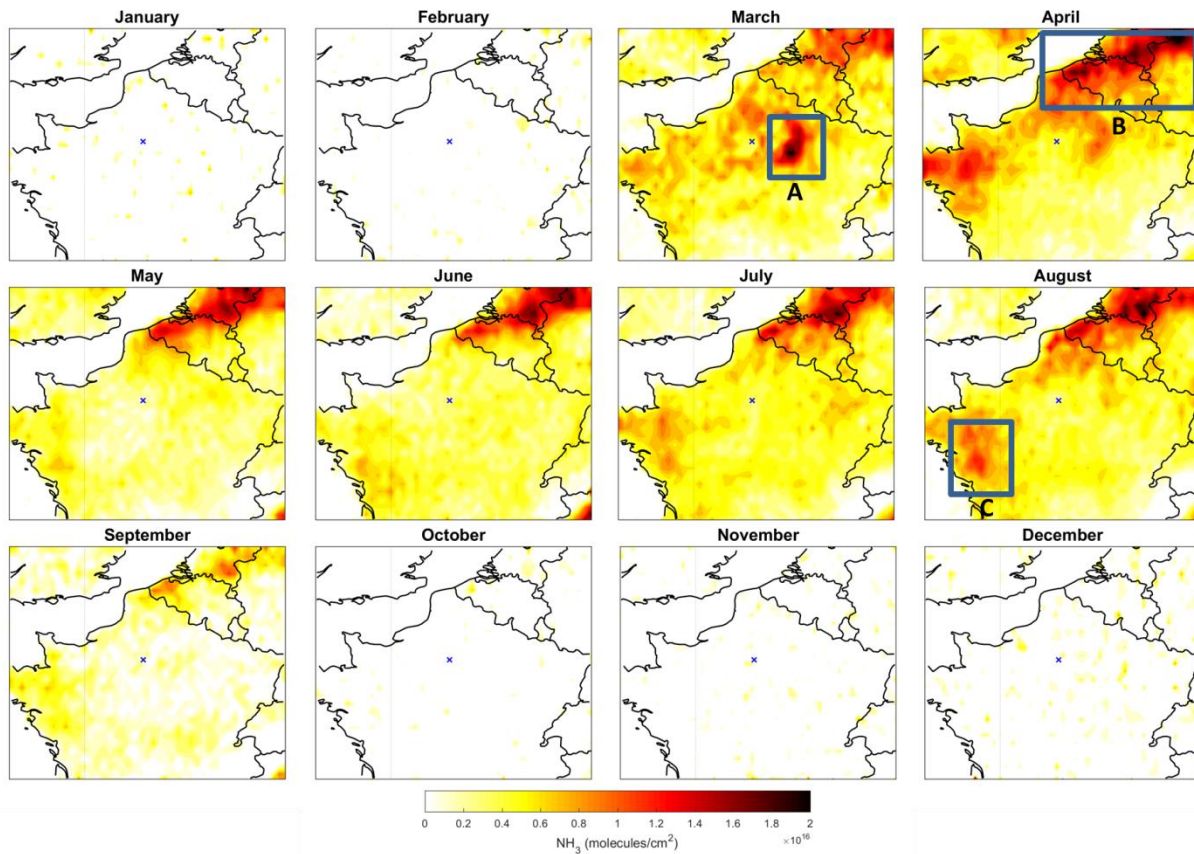
930 Zhu, L., Henze, D. K., Cady-Pereira, K. E., Shephard, M. W., Luo, M., Pinder, R. W., Bash, J. O., and
931 Jeong, G.: Constraining U.S. ammonia emissions using TES remote sensing observations and the
932 GEOS-Chem adjoint model, *J. Geophys. Res.-Atmos.*, 118, 3355–3368, doi:10.1002/jgrd.50166,
933 2013.

FIGURES



935

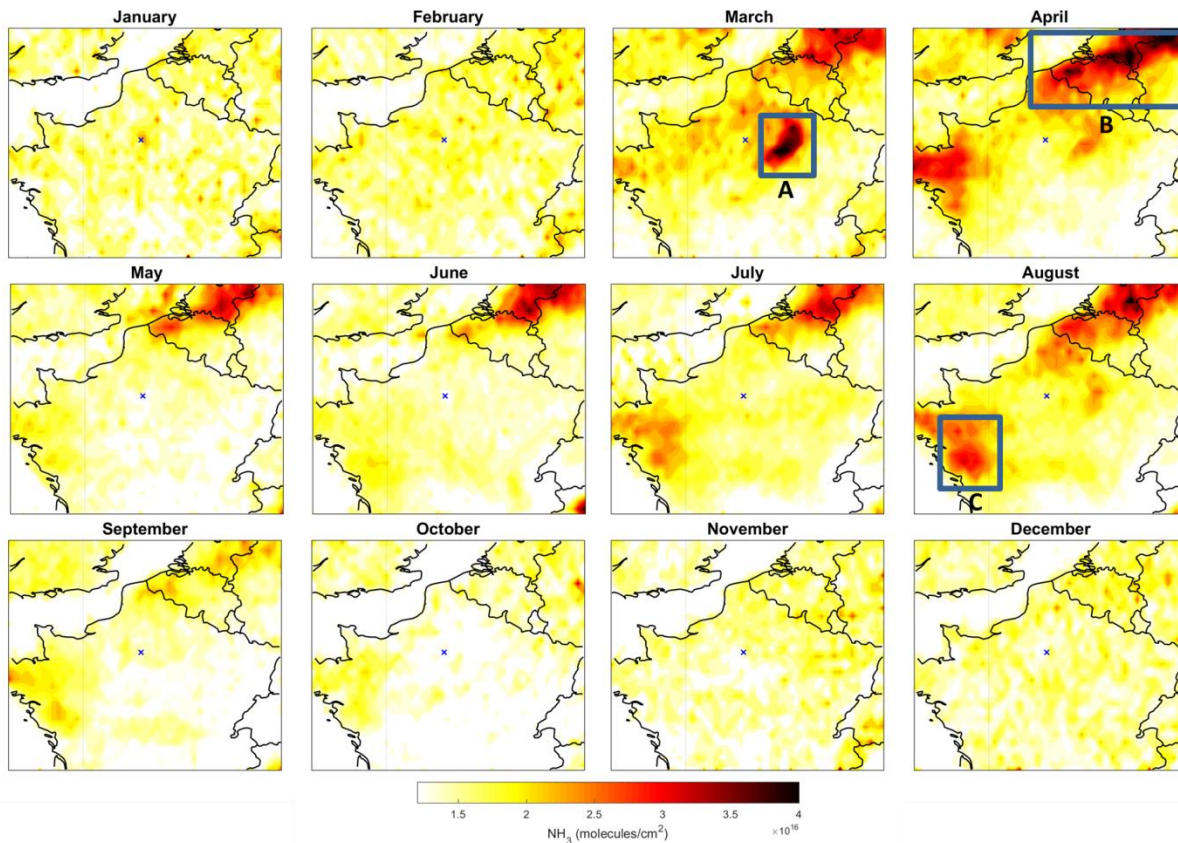
936 Figure 1: Region of analysis: 400 km radius-circle around the Paris megacity and 100 km around
937 Paris. The latter is representative of the Ile-de-France (IdF) region where the Airparif PM
938 observational network is located. Black points are the locations of the Airparif stations
939 measuring hourly PM_{2.5} concentration at the surface. The black (blue) box delimitates the IdF
940 region in which the IASI NH₃ (ECMWF) data have been considered. The overlay represents NH₃
941 emissions (in Mg per year and per cell of 0.1°x0.1°) derived from the EMEP inventory for 2015.



942

943 Figure 2: Monthly means of NH₃ total columns (molecules/cm²) derived from 10 years (2008-
 944 2017) of IASI NH₃-retrieved columns. The blue cross indicates Paris location.

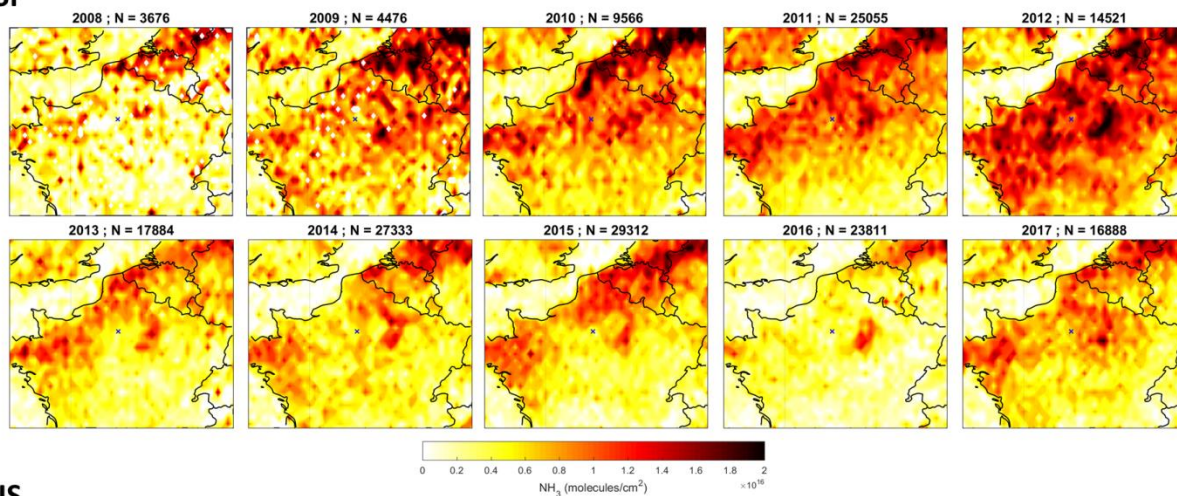
945



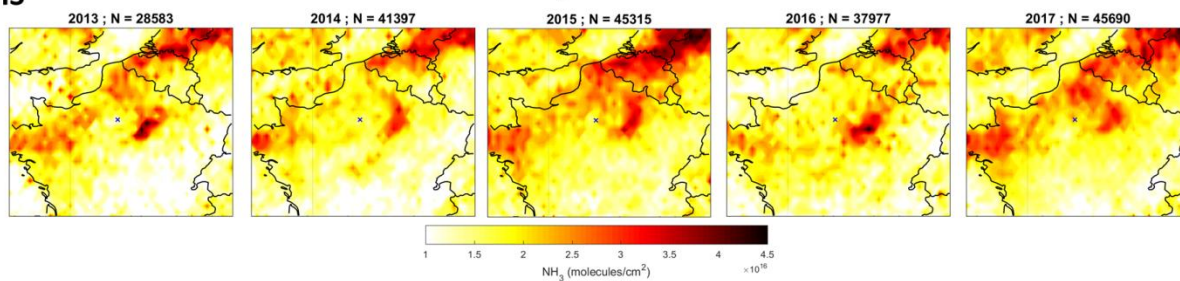
946

947 Figure 3: Monthly means of NH₃ total columns (molecules/cm²) derived from 5 years (2013-
 948 2017) of CrIS NH₃-retrieved columns. The blue cross indicates Paris location.

IASI

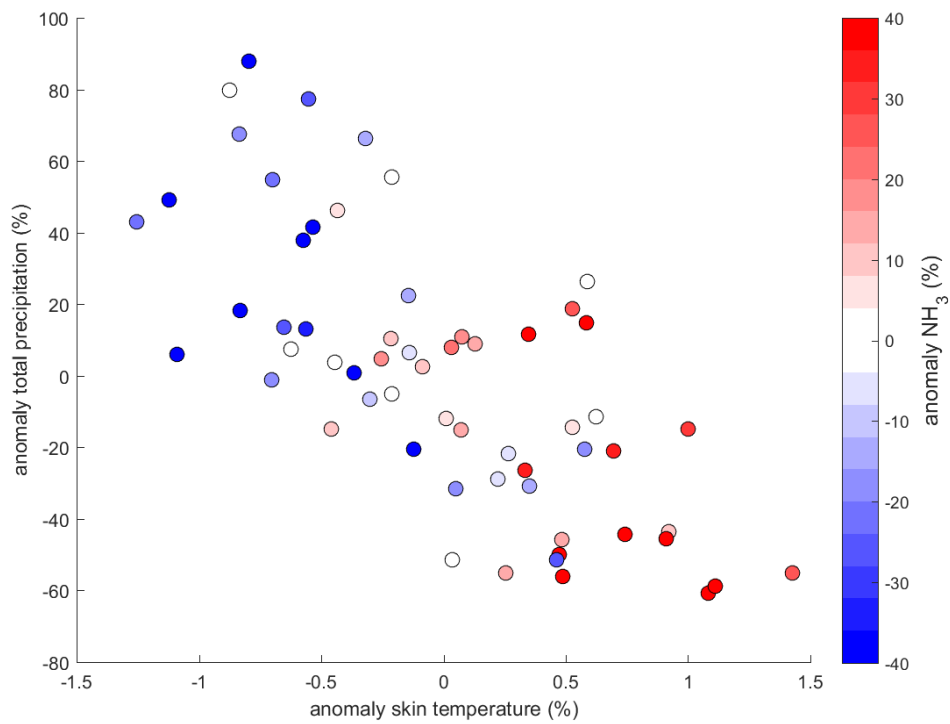


CrIS

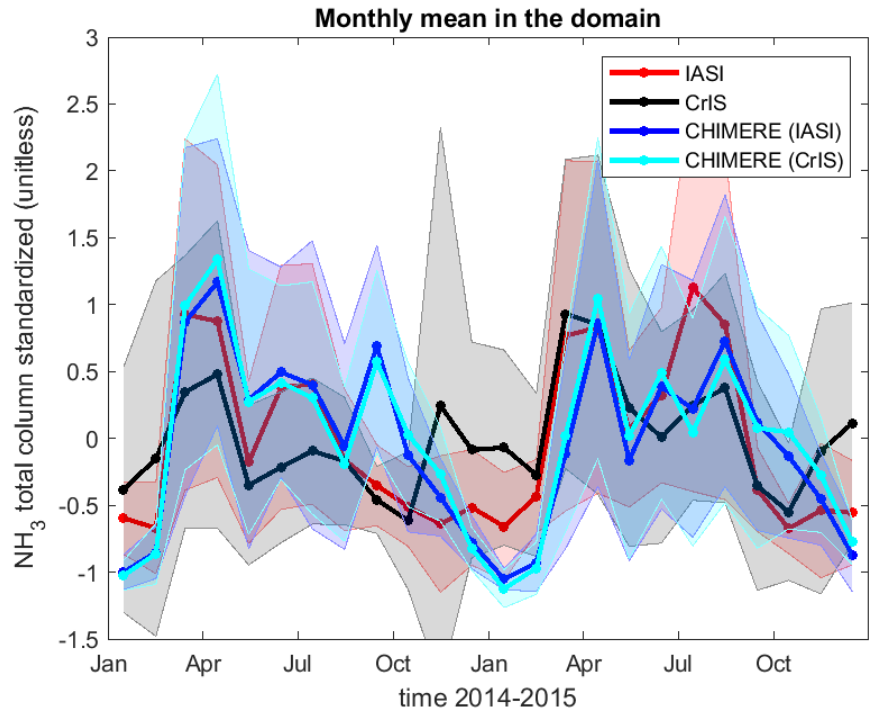


949

950 Figure 4: Maps of monthly mean NH₃ total columns (molecules/cm²) in March-April period
951 derived from IASI from 2008 to 2017 and CrIS from 2013 to 2017.

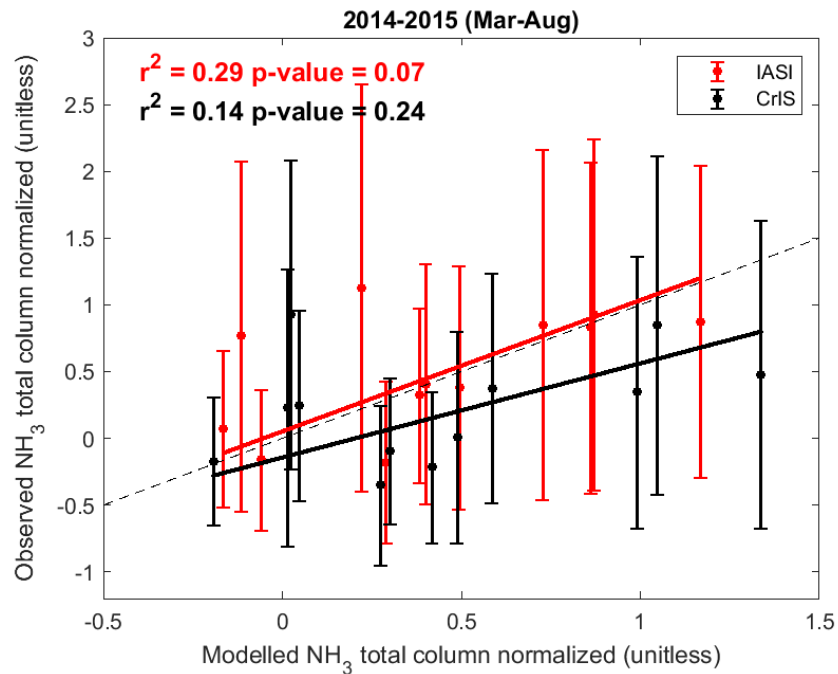


952
 953 Figure 5: Scatter plot of monthly mean anomaly (relative to the 10-years – 2008 to 2017 -
 954 monthly average) of total precipitation versus skin temperature derived from ECMWF from
 955 March to August in the domain, and color coded by the NH₃ total columns anomaly derived
 956 from IASI.



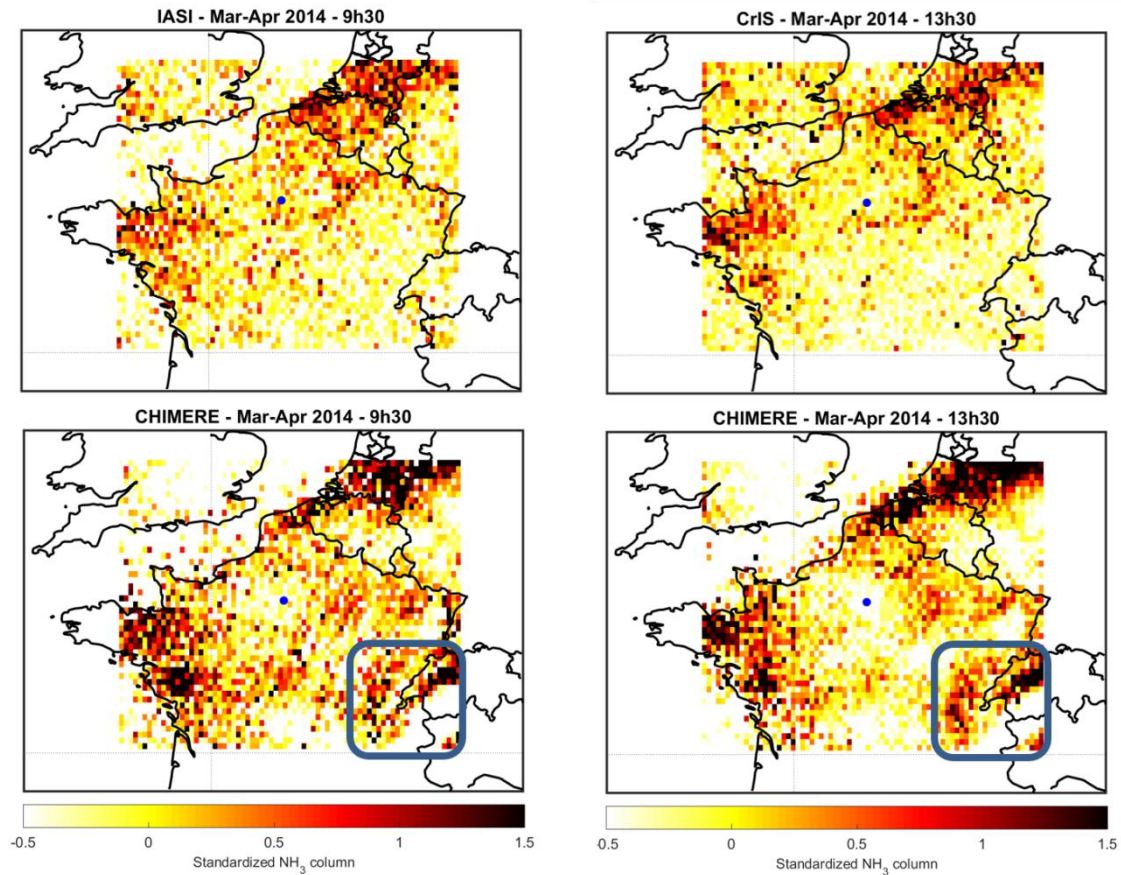
957

958 Figure 6: Standardized monthly mean concentrations derived from IASI (red), CrIS
 959 (black), CHIMERE sampled at IASI overpass time and space (blue) and CHIMERE sample at CrIS
 960 overpass time and space (cyan) for 2014 and 2015. Shaded areas correspond to the one-sigma
 961 standard deviation around the means.



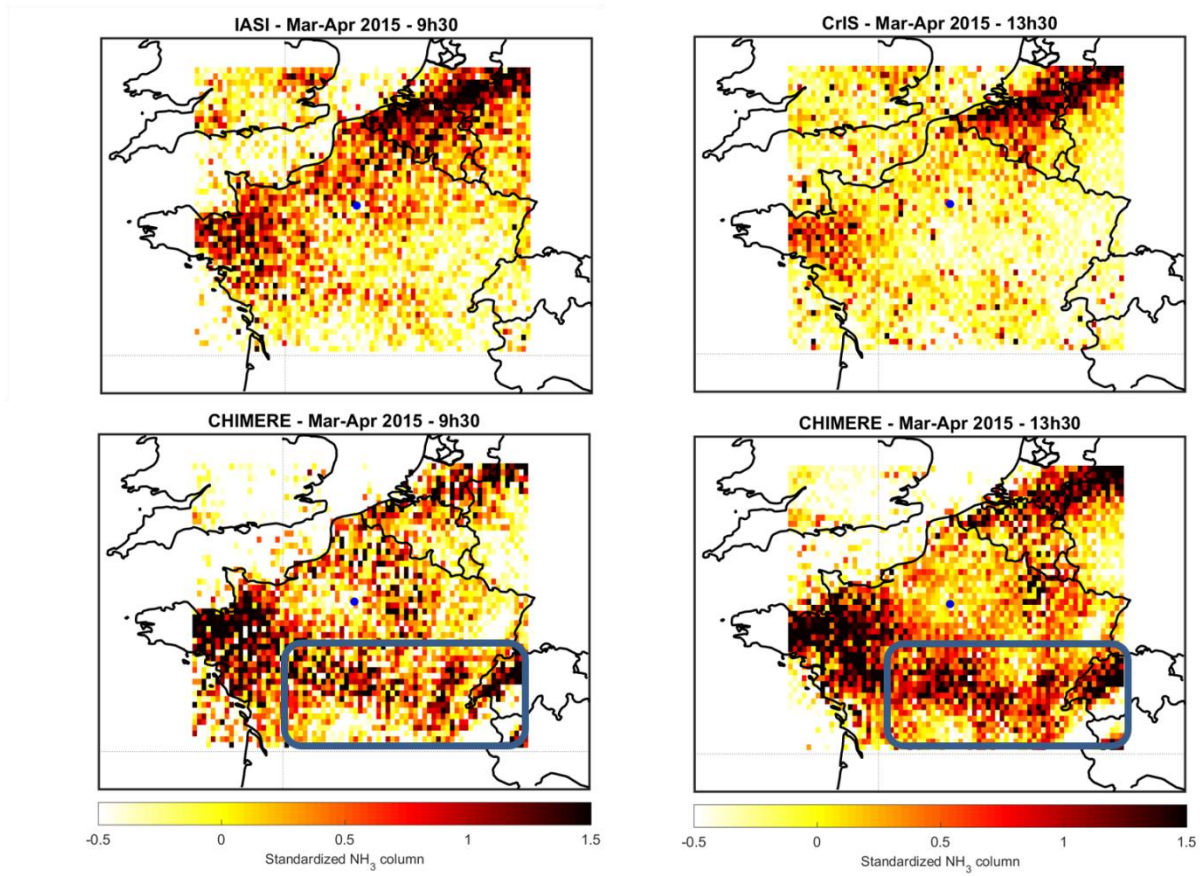
962

963 Figure 7: Correlation plots between monthly means NH_3 standardized concentrations derived
 964 from satellite observations (IASI in red and CrIS in black) and the CHIMERE outputs for the
 965 March to August months of 2014 and 2015. The 1:1 line is represented in the dashed line. Error
 966 bars represent the one-sigma standard deviation around the monthly means.



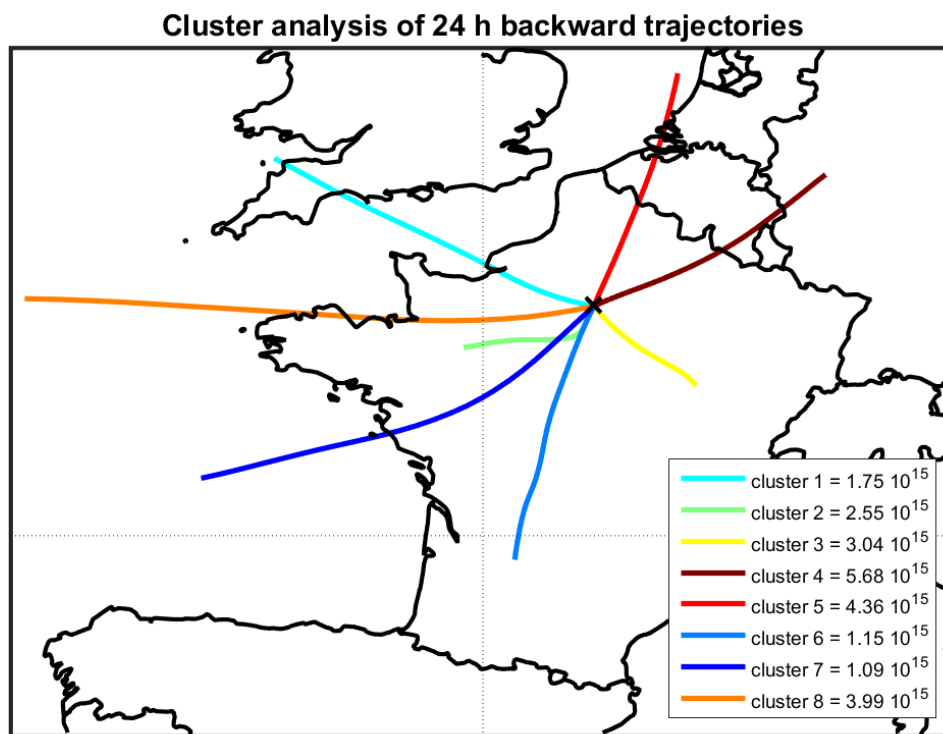
967

968 Figure 8: Standardized NH_3 column derived from the satellite instruments (IASI = top left panel,
 969 and CrIS = top right panel) and the corresponding NH_3 column derived from the CHIMERE model
 970 (coincident with IASI – bottom left panel, and coincident with CrIS – bottom left panel) for
 971 March-April 2014. Blue dots indicate Paris location.



972

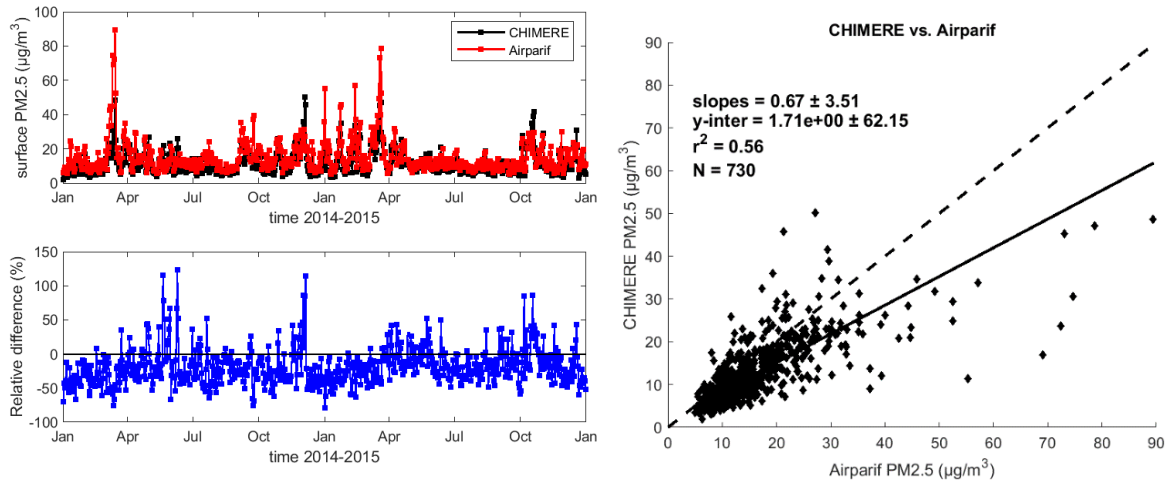
973 Figure 9: Same as Figure 7 but for March-April 2015.



974
 975 Figure 10: Cluster analysis of 24-h backward trajectories arriving in spring in Paris (from
 976 February 15th to May 15th for the 2013-2016 period) using HYSPLIT-4 model obtained from the
 977 NOAA Air Resources Laboratory. Mean trajectories of the 8 clusters are shown in different
 978 colors, associated with the NH₃ concentrations measured by IASI in the IdF region (in
 979 molecules/cm⁻²).

980

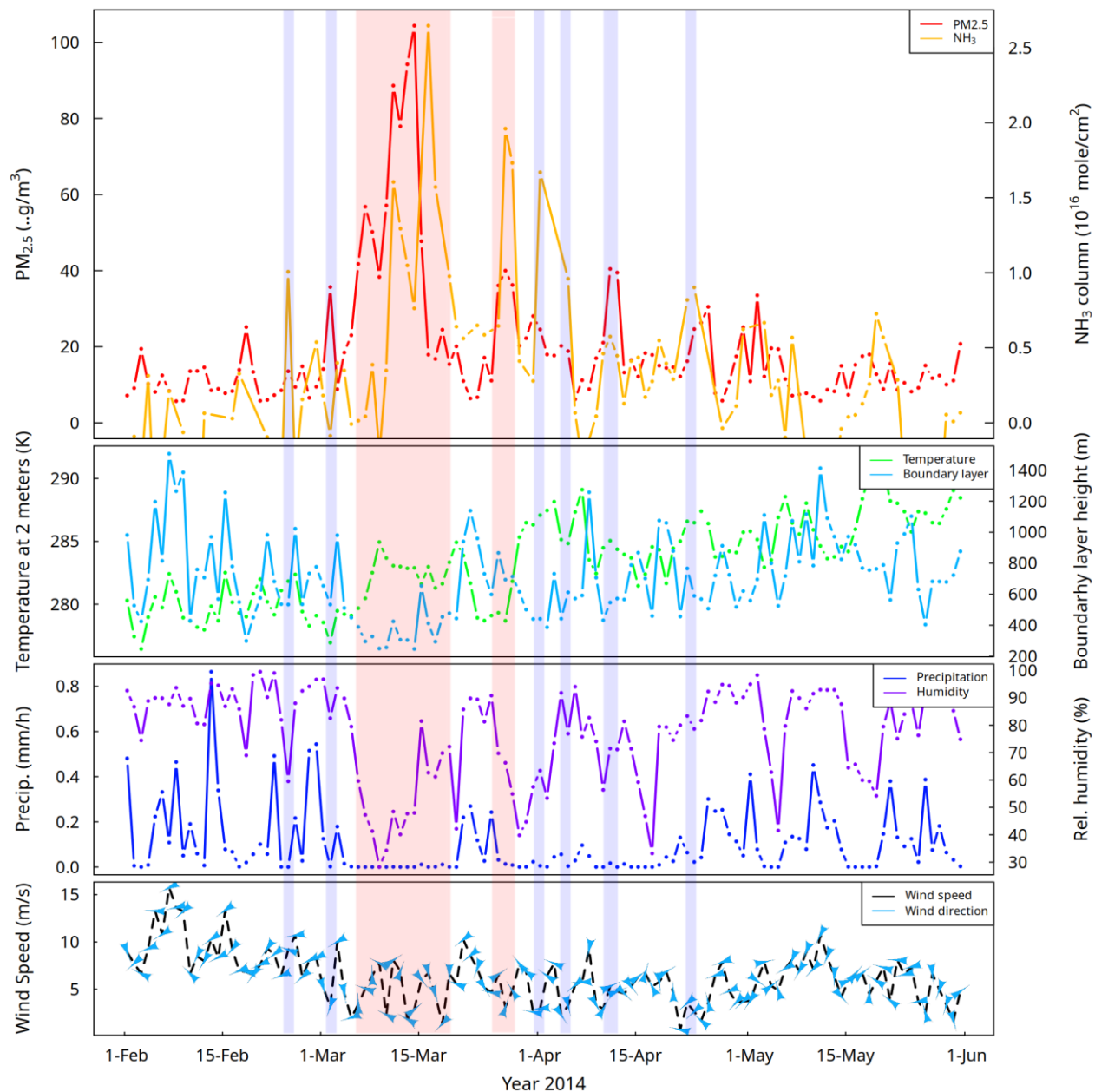
981



982

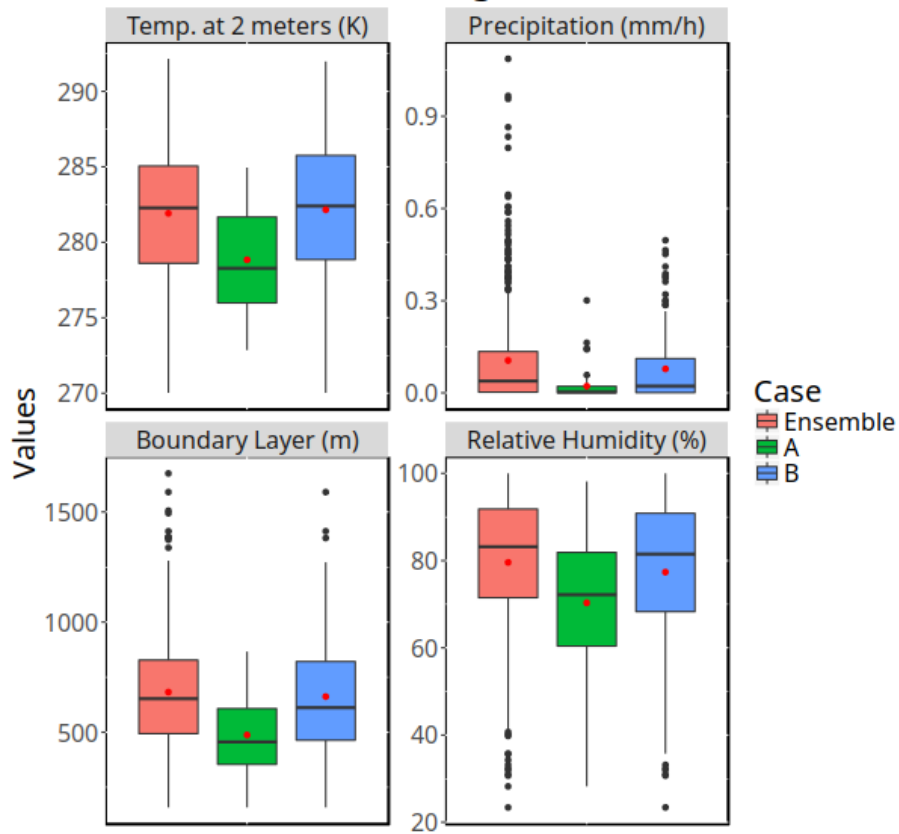
983 Figure 11: Comparison between PM_{2.5} concentrations derived from the Airparif network and the
984 CHIMERE model outputs. Left panel: time serie of the daily mean PM_{2.5} concentrations (in
985 µg/m³) observed at the surface with the Airparif network (red) and calculated with the CHIMERE
986 model (black), associated with relative differences (in %) calculated as model-observations for
987 2014 and 2015. Right panel: correlation plots between daily mean PM_{2.5} concentrations derived
988 from the CHIMERE model versus the Airparif network.

989



990
 991 Figure 12: Average concentrations of NH_3 total columns derived from IASI (in molecules/cm²;
 992 orange, upper panel) and $\text{PM}_{2.5}$ derived from the Airparif network selected within 2 hours from
 993 the IASI overpass (in $\mu\text{g}/\text{m}^3$; red, upper panel) for 2014 as example. Periods of simultaneous
 994 (independent) enhancements of NH_3 and PM concentrations are represented with red (blue)
 995 areas, i.e. case A (case B). Temperature at 2 meters (in Kelvin; green, upper middle panel),
 996 boundary layer height (in meter; blue, upper middle panel), precipitation (in meter; dark blue,
 997 lower middle panel), relative humidity (in percent; purple, lower middle panel), and wind speed
 998 and directions (lower panel) derived from the ECMWF ERA-5.
 999

Influence of Meteorological Parameters



1000
 1001 Figure 13: Statistical distributions of meteorological parameters corresponding to case A, case B,
 1002 and all observations derived from 2013 to 2016. The medians and the quartiles are presented by
 1003 center lines and borders of the boxes, respectively. The mean values are indicated by red points,
 1004 and the extreme values (i.e. those beyond $Q1 - 1.5 \text{ IQR}$ and $Q3 + 1.5 \text{ IQR}$) by black points. The
 1005 IQR is the "interquartile range", and it equals to $Q3 - Q1$ where $Q3$ and $Q1$ are the 75th and 25th
 1006 percentiles. Setting the thresholds at $Q1 - 1.5 * \text{IQR}$ and $Q3 + 1.5 * \text{IQR}$ is a common practice to
 1007 determine outliers.

1008

TABLE

Satellite	Overpass time (LT)	Time coverage	Nadir spatial resolution (km)	Spectral range (cm ⁻¹)	Spectral resolution (cm ⁻¹)	Spectral Noise* (K) @270K @ 970 cm ⁻¹	References
IASI Metop-A/B	9.30 (AM/PM)	2006-present	12	645–2760	0.5 (apodized)	~0.2	Clerbaux et al., 2009
CrIS Suomi-NPP	1.30 (AM/PM)	2011-present	14	645–1095; 1210–1750; 2155–2550	0.625; (unapodized)	~0.05	Zavyalov et al., 2013

*Spectral noise comparison values in main ammonia spectral region (~970 cm⁻¹) obtained from Zavyalov et al., 2013.

1010 Table 1: Instrumental specifications for the IASI and CrIS satellite instruments.